Stability of Reduced Carbon in the Mantle

A THESIS
SUBMITTED TO THE FACULTY OF THE GRADUATE SCHOOL
OF THE UNIVERSITY OF MINNESOTA
BY

Patrick Timothy Hastings Jr.

IN PARTIAL FULFILLMENT OF THE REQUIREMENTS
FOR THE DEGREE OF
MASTER OF SCIENCE

Marc Hirschmann

January 2013

Acknowledgements

The authors would like to thank Ellery Frahm for his assistance on the EMPA and the National Science Foundation for funding this research under award number EAR1119295.

Dedication

I would like to dedicate this thesis to my wife, my mother and my father for their endless encouragement, guidance and support. Also my children who make my life complete.

Table of Contents

List of tables

List of figures

Introduction

Cycling of carbon between Earth's surface reservoirs and deep interior affects the dynamics, geochemistry, and geophysics of the interior, therefore influencing the locus of melting, geochemical differentiation, and physical properties (**Dasgupta and Hirschmann, 2010**). Perhaps the largest reservoir for the storage of carbon is the deep interior. The mass of carbon in that reservoir likely exceeds 12×10^{23} grams (**Sleep and Zahnle, 2001; Hirschmann and Dasgupta, 2009; Dasgupta and Hirschmann, 2010**). Determining which carbon-bearing phases are stable in the mantle is important for understanding the cycling of carbon between reservoirs. Which phases are stable may affect the chemical and physical properties of the mantle as well as the fluxes between reservoirs. The determination of these stable phases that host carbon in the mantle is essential to understand the cycling of carbon between Earth's reservoirs (**Dasgupta and Hirschmann, 2010**).

Stable carbon-bearing phase assemblages vary with depth and oxygen fugacity. Carbon in the upper mantle has been suggested to reside in carbonates (**Dasgupta and Hirschmann, 2010**). Experiments suggest that with increasing depth the mantle becomes more reduced (**Ballhaus et al. 1990; O'Neill et al. 1993; McCammon, 2005; Frost and McCammon, 2008; Rohrbach et al. 2007; 2011; Goncharov et al. 2012**). This suggests that in the deep upper mantle, transition zone, and lower mantle, carbon may exist in the reduced form. The stability of phases containing reduced carbon influences the locus of silicate melting in the mantle (**Taylor and Green, 1987; Stagno and Frost, 2010**), the occurrence of metal-rich melts, the distribution of siderophile and other elements (**Chabot et al. 2008**), the origin of diamond, and physical properties

such as conductivity. Carbon in the reduced mantle is often thought to take the form of diamond, and in oxidized zones to take the form of carbonates (**Walter et al. 2008**).

Frost et al. (2004), Rohrbach et al (2007; 2011) and Frost and McCammon (2008) suggest that the mantle is saturated in metal (with an abundance of up to ~1 wt. %) below ~250 km. Metal becomes stable when Fe^{3+} is incorporated into the garnet structure (**Frost et al. 2004; Rohrbach et al. 2007; 2011; Frost and McCammon, 2008**). The first appearance of the metallic phase occurs at a pressure of ~8 GPa (**Rohrbach et al. 2007; 2011; Frost and McCammon, 2008**). Since Ni metal is more stable under oxidizing conditions than Fe (**Campbell et al. 2009**), the first alloy to precipitate is Ni-rich, with an Ni/Fe ratio that is large compared to those in coexisting olivine (**Seifert and O'Neill, 1988; Hirschmann and Ghiorso, 1994; Holzheid and Grove, 2005**). Frost and McCammon (2008) calculated that the first alloy to precipitate has the composition $Fe_{0.4}$-$Ni_{0.6}$ and an abundance of ~0.1 wt. %. The alloy becomes gradually more Fe-rich and its mass fraction increases with depth. An Fe-rich alloy and diamond do not coexist in thermodynamic equilibrium. (**Strong and Chrenko 1971; Chipman, 1972; Dasgupta and Walker, 2008; Lord et al. 2009; Nakajima et al. 2009**). Thus, if diamond is the chief host of C in the lower mantle, then no Fe-rich alloy can be present. If Fe-rich alloy is present, iron carbide will form as a reaction product. However, for high bulk C contents (such as OIB-source mantle with 30-500 ppm, **Dasgupta and Hirschmann, 2010**) and Ni-rich alloy, diamond may be present in addition to the alloy, whereas for low bulk C contents (5-30 ppm in MORB-source mantle) and Fe-rich alloy (Frost et al. 2004), all of the carbon will dissolve in the metallic phase.

The solubility of carbon in metal alloy defines the phase boundary in the system Fe-Ni-C. The solubility, and hence the phase boundary, will vary with the pressure and composition (Ni/(Fe+Ni)). Additionally, the carbide + Fe-rich metal phase assemblage may not be stable over large depth intervals along a mantle adiabat, as low eutectic temperatures allow formation of a carbide melt (**Strong and Chrenko, 1971; Wood, 1993; Chabot et al. 2008; Lord et al. 2009; Dasgupta and Hirschmann, 2010**). However, the metallic phase metal will take the form of an Fe-Ni alloy, rather than pure Fe. The presence of Ni has an important influence on the storage of reduced carbon in the mantle. Ni-enrichment will increase the eutectic temperature, limiting the formation of a carbide melt (**Strong and Chrenko, 1971**). The solubility of C is lower in more Ni-rich alloys (Romig and Goldstein, 1978). Unlike Fe-rich alloy, Ni-rich alloy can coexist with diamond, as Ni-rich carbides are not stable (**Strong and Hanneman, 1967**), and so Ni-enrichment destabilizes crystalline carbides relative to diamond + alloy.

Evaluation of C-bearing phase stability in the mantle requires characterization of the Fe-Ni-C ternary system at relevant temperatures and pressures. The phases that could possibly store carbon in the reduced mantle include graphite, diamond, Fe-Ni carbide, Fe-Ni alloy, and melt. The stability of these phases (and their combinations) almost certainly varies with depth, oxygen fugacity, and carbon inventory, leading to multiple possible variations in the predominant carbon-bearing phase with depth in the mantle (**Figure 1**). It is remarkable that there is such uncertainty regarding the principal hosts of carbon in the reduced mantle. Determining the phase relations of C-bearing phases is one of the key challenges associated with understanding the deep Earth carbon cycle.

In this study, we experimentally examine the Fe-Ni-C system from 3 to 7 GPa and 1000-1400°C, to determine C solubility as a function of composition in Fe-Ni alloy and to produce a phase diagram for the Fe-Ni-C ternary. Where possible, we document compositions of melts coexisting with alloys and carbides. Even though no metallic phase is likely to be present in the mantle at pressures below 6 GPa (**Rohrbach et al. 2007; 2011; Frost and McCammon, 2008**), the experiments explore the effects of pressure and temperature on the reactions of interest and expand on previous work (Strong and Chrenko, 1971; Romig and Goldstein 1978).

Methods

Starting Materials

starting materials were prepared, all with 5 wt.% C and 95% Fe+Ni, with the proportion of Fe/Ni ranging from 0 to 1, with 6 intermediate compositions (Ni/(Fe+Ni)=1/7,2/7,etc.). Starting materials were synthesized from 99.9% Fe and 99.9% Ni powders (Alfa-Aesar) and reagent grade graphite powder (Carbone of America). All starting materials were ground in a mortar and pestle for 2 ½ hours under ethyl alcohol. Starting materials used to synthesize Fe_3C and Fe_7C_3 standards for electron microprobe analyses were prepared using the same procedure from stoichiometric mixtures of Fe and C.

Experiments at 3 GPa and 1000-1250 °C were performed in an end-loaded piston cylinder apparatus at the University of Minnesota using the experimental assemblies, procedures, and calibrations described by Xirouchakis et al. (2001). Starting materials were pressed into disks made from 4-bore Al_2O_3 thermocouple insulators. The

Al_2O_3 discs, which we call multicapsules, were ~1.7 mm thick and had an external diameter of ~3.5 mm (**Figure 2**). These capsules were capped on top and bottom with solid alumina disks, resulting in a total capsule length of 1 mm. The multicapsules allow simultaneous investigation of 4 separate bulk compositions in each experiment. In contrast to more conventional metal or MgO capsules, the alumina provides an effectively chemically inert container for Fe-Ni-C compositions. We also avoid the use of graphite capsules, which would cause difficulties at pressures where diamond nucleation is possible. A time series at 1, 12, 24, and 72 h was run to determine the time required to produce equilibrium phase compositions and textures. Based on textural and quantitative analysis it was estimated that equilibrium was attained within 24 h (**Figure 3**). Experiments at 5 to 7 GPa and 1200-1400°C were performed in a 1000 ton Walker-style octahedral multianvil (MA) using a 12 mm truncated edge length (12 TEL) assembly with cast MgO/Cr_2O_3 octahedra and gaskets. Additional details are given in Dasgupta et al. (2004). Temperature was controlled with a type D thermocouple. Thermocouple EMF was not corrected for the effect of pressure.

The Fe_3C carbide standard was synthesized in the piston cylinder at 1200°C and 2 GPa using an assembly similar to the 3 GPa phase equilibria experiments, but without a capsule. The Fe_7C_3 was synthesized in the MA device at 7.5 GPa and 1350°C using the "large volume" 12 TEL assembly described by Withers et al. (2011).

Analytical Technique

Experiments were analyzed using the JEOL JXA-8900 electron microprobe analyzer (EMPA) at the University of Minnesota. WDS analysis of carbon was performed using a multilayer crystal (LDE2 with 2d = 9.7nm). The samples and the

standards were polished to a finish of 1 µm and pressed in indium. As the run products are conductive, neither standards nor unknowns had a conductive coating. Both ends of the samples and standards were polished to ensure electrical contact through the bottom of the capsules. Carbon analysis using EMPA can be challenging due to ubiquitous carbon and hydrocarbon contamination in the microprobe, arising chiefly from vacuum greases and oil (**Robaut et al., 2006; Dasgupta and Walker, 2008**), and due to the effects of bonding on C excitation energies (**Bastin and Heijligers, 1986**). To minimize carbon contamination and correct for bonding effects we established an analytical protocol based on techniques described by Dasgupta and Walker (2008) and Stewart (2006).

Analytical Standards

Analysis of carbon by EMPA requires both primary and secondary standards, owing to the delicacy of carbon analyses and in particular the sensitivity of C x-ray peak location and shape to bonding environment (**Bastin and Heijligers, 1986**). We chose synthetic Fe_3C (6.67 wt. % C) as our primary carbon standard because the unknown phases were either quenched carbide, Fe-Ni alloy or a Fe-Ni melt, all of which have metal-carbon bonding similar to that of carbide. The secondary standards were synthetic Fe_7C_3 (8.43 wt. % C), NIST 663 steel (0.57 wt. % C), and NIST Fe metal (99.995 wt. %). Note that most NIST steel standards are not satisfactory as standards, as carbon is heterogeneously distributed in C-rich phases. Additionally, steel standards commonly have other metals such as Cr and Mn, which produce interferences with C K_α emissions (Dasgupta and Walker 2008). Backscatterered electron (BSE) imaging confirmed that NIST 663 is homogeneous. The stoichiometry and homogeneity of

carbide standards, synthesized at high pressure, were verified by powder XRD and BSE imaging. Standards for Fe and Ni analyses were Fe metal (99.995 wt. %) and Ni metal (99.995 wt. %), respectively. WDS scans were performed on all standards to determine a correction for any peak and background overlap between C, Fe and Ni. Matrix corrections were made using ZAF. A single channel analyzer (SCA) scan was executed to help eliminate low and high-energy noise and optimize our LDE2 crystal.

The carbon contamination level in the microprobe vacuum chamber is time dependent owing to its origin in the cracking of hydrocarbons in the path of the electron beam (**Robaut et al. 2006; Dasgupta and Walker, 2008**). To minimize C contamination (**Bastin and Heijligers, 1986; Robaut et al., 2006**), we used a liquid N_2 cold-finger close to the EMPA stage, which was refilled every 3 hours during each analytical session. We also followed the procedure of Stewart (2006) and Dasgupta and Walker (2008), tracking the rate of C counts with time in the analysis. We found an optimum counting time of 10 s on the peak and 5 s on the background for our instrument.

To determine the optimum analytical conditions, we monitored the intensity of C counts as a function of beam voltage and current whilst analyzing the Fe3C standard. Optimum peak/background ratios of 20-22 were found for voltages of 9-12 kV and a current of 80 nA (**Figure 4**). Consequently, we analyzed standards and unknowns at 11 kV and 80 nA to ensure Fe and Ni X-ray excitation. The resulting peak/background ratio compares favorably with maximum values of 7.5 and 13 found by Stewart (2006) and Dasgupta and Walker (2008), respectively. A focused beam was used to analyze sub-solidus alloy, while a 20 μm beam size was used to analyze quenched melt. All

melt compositions were normalized to 100%, since the large beam size resulted in excitation of Al_2O_3.

Employing the beam conditions described above, repeated analyses of the pure Fe standard every 2 hours during our sessions (waiting 30 minutes after liquid N_2 was added to the cold finger) revealed a persistent carbon contamination of 0.48±0.08 wt.% (n=352, 1 s.d.) (**Figure 5**). This blank is similar to that reported in previous studies (**Hirayama et al. 1993; Wood, 1993; Dasgupta and Walker, 2008; Nakajima et al. 2009; Righter et al. 2009**) and reported carbon concentrations have had this amount subtracted from analyzed values. The small inter-session variability of the blank gives us confidence that reported C concentrations are precise to <0.1 wt. %.

Results

Texture and Phase Composition

At 3 GPa and 1000°C and at 5 and 7 GPa and 1200°C the entire range of Fe-Ni alloys are solid. Both alloy + Fe_3C phases (**Figure 6**) exist in the range of Ni/(Fe+Ni) = 0 to 0.29, while the more Ni rich samples produce alloy + graphite (**Figure 7**). All experiments have some Al_2O_3 present as a polishing artifact from the capsules. Melting was determined by textural analysis. Dendrite (**Figure 8**) or acicular (**Figure 9**) textures are interpreted as evidence of melting. At 3 GPa for Ni/(Fe+Ni) = 0 to 0.35 melt is present at 1250°C. These melts are believed to be 100 % melted and upon quenching, Fe_3C crystals grow leaving behind a residue alloy (**Figures 8 & 9**). No graphite was observed in these melt-present experiments. Quenched melts with dendritic textures have some Ni present, while those with acicular textures are pure Fe. At 5 and 7 GPa

and 1400°C the entire range of Ni/(Fe+Ni) = 0 to 1 are molten. Ni/(Fe+Ni) = 0 to 0.42 melt textures are dendritic for Ni present and acicular for pure Fe. Ni/(Fe+Ni) = 0.57 to 1 melt textures are globular. (**Figure 10**).

Carbon Solubility in Fe-Ni Alloy

All experiments analyzed by EMPA are listed in Table 1. The solubility of carbon in Fe-Ni alloy at 3, 5 and 7 GPa starts at ~1 wt.% C in a pure Ni alloy and decreases with increasing Fe until around Ni/(Fe+Ni)=0.6, which ~0.3 wt.% C is soluble. At this point the C solubility begins to increase with increasing Fe (**Figure 11**) until it reaches ~2 wt.% C in pure Fe. All results are similar to other experimental data (**Figure 11**). An average of 5 wt. % C was dissolved in melting experiments (**Figure 12**). This value matches our bulk composition, so represents a minimum bound to the solubility of C. Previous experiments show that up to 6-8 wt.% C could be dissolved in Fe melts (**Dasgupta and Walker 2008**).

Phase relations in Fe-Ni-C Ternary

Phase diagrams were constructed based on our experimental results (**Figures 13-18**). At 3GPa and 1000°C (**Figure 13**) all experimental products are solid. As the temperature increases to 1250°C (**Figure 14**) Fe-rich experiments with up to Ni/(Fe+Ni)=3/7 produce melts, but as the Ni concentration increases the melting temperature increases. A three phase field must lie between alloy compositions of Ni/(Fe+Ni)=3/7 and 4/7. As the pressure rises to 5 and 7 GPa at 1200°C (**Figures 15 and 17**) the Fe-rich experiments are still molten, although at 7 GPa the Ni

concentrations of the melts are lower than those in the 5 GPa experiments (**Figure 19**). At 1400°C in the 5 and 7 GPa experiments (**Figures 16 and 18**) all of the experiments produce melt.

Discussion

Carbon solubility

Our experiments show that metal can incorporate varying amounts of carbon with changing alloy composition, which is consistent with the 1 atmosphere experiments by Wada 1971, Ramathan 1980 and 5 GPa experiments by Chabot 2005 (**Figure 11**). Rohrbach et al. (2007; 2011) suggest that metal saturation occurs at approximately 8 GPa and that the first alloy to form is Ni rich with a composition close to $Fe_{0.4}Ni_{0.6}$ with a modal abundance of 0.1wt.% and increases to approximately 1 wt.% modal abundance at 25 GPa with a composition close to $Fe_{0.88}Ni_{0.12}$ (**Figure 20**). Assuming a linear trend of changing alloy composition and modal abundance with depth, a carbon saturation curve was drawn (**Figure 21**) based on our C solubility in solid alloy data. In MORB source mantle with 10–30 ppm C (**Figure 21 boxed area**), a small proportion of the carbon can be stored in the alloy with the remainder present as diamond. As the alloy composition becomes more Fe-rich, increasing to as much as ~1 wt. % Fe rich metal in the lower mantle(Frost et al. 2004), then all of the carbon will dissolve in the alloy (**Figure 22a**). For enriched mantle where the carbon concentration could be as high as 500ppm, all of the carbon would be stored in Fe-rich alloy in the lower mantle (**Figure 22b**), until a $(Fe,Ni)_3C$ is stabilized. This would happen in the very deep mantle because $(Fe,Ni)_3C$ cannot contain more than ~17 wt.% Ni, so the

increasing Ni content of the metal will inhibit Fe_3C formation and stabilize Fe-Ni alloy. However, the most likely form of carbide to exist in the lower mantle is $(Fe,Ni)_7C_3$. Higher pressure experiments are needed to determine the solubility of Ni in $(Fe,Ni)_7C_3$.

The existence of the carbide and Fe eutectic point indicates that Fe–Ni metal saturation could stabilize a carbon-bearing melt (**Hirayama 1993; Fei 2007; Andrault 2009; Lord et al. 2009; Nakajima et al. 2009 and Dasgupta and Hirschmann 2010**) . The eutectic point at 5 and 7 GPa lies below the mantle geotherm (**Figure 23**), suggesting that carbon would be dissolved in a metallic melt with a composition close to the eutectic composition of $Fe_{0.4}Ni_{0.6}$. The mantle geotherm was redrawn after Stixrude and Lithgow-Bertelloni (2007). As the alloy composition becomes more Fe-rich with depth, we project that the alloy eutectic will lie below the mantle geotherm. According to our experiments these metallic melts can incorporate significantly more carbon (**Figure 12**) than solid alloy. A carbon saturation curve was drawn (**Figure 24**) based on the solubility of C in melt. All of the 5 wt. % carbon in our experiments is dissolved in the melt, which means that the solubility of carbon in melts must be greater than 5 wt.% (**Figure 24**). Experiments suggest that 6-8 wt.% carbon is soluble in molten Fe depending on temperature (**Chabot et al. 2005; Dasgupta and Walker 2008**). So for MORB source mantle, all of the carbon would be stored in melt (**Figure 25a**). Otherwise for enriched source mantle, some of the carbon would be stored in diamond + melt, but with increasing depth the carbon would dissolve increasingly in Fe-rich melt in the lower mantle (**Figure 25b**). The dissolution of carbon in the melt wil depend on the shape of the curve that constrains the changing alloy composition and modal

abundance with depth (**Figure 13**), which has, as a first approximation, been assumed to be linear.

Diamonds in the mantle

Diamonds from the depths of the lower mantle, as well as the transition zone, are found in several places. Inclusions in these diamonds consist of minerals that could form only at transition zone and lower mantle depths (**Stachel, 2001; Kamansky et al. 2011; Walter et al. 2011**). This is inconsistent with experiments that suggest Fe metal saturation occurs in the mantle (**Frost et al. 2004; Rohrbach et al. 2007; Frost and McCammon, 2008 and Rohrbach et al. 2011**) and our experiments. However, the diamonds in these localities are thought to be associated with subduction materials (**Tappert et al. 2005 and Walter et al. 2011**) and ascend through kimberlites and lamprorites. These diamonds may not be representative of the bulk mantle. Alternatively, Fe metal saturation may somehow be prohibited. Lastly, the increase in mode of alloy from 0.1 wt.% to ~1 wt.% may be overestimated. If metal alloy mode is lower than these estimates, some carbon would be stored in a melt and/or carbide, but in the remainder would form diamond. This is consistent with mineral inclusions of Fe-carbide (**Kaminsky et al. 2011**) and iron alloy (**Jacob et al. 2004 and Walter et al. 2008**) found in diamond.

References

Andrault, D., Bolfan-Casanova, N., Ohtaka, O., Fukui, H., Arima, H., Fialin, M. and Funakoshi, K., (2009). Melting diagrams of Fe-rich alloys determined from synchrotron *in situ* measurements in the 15–23 GPa pressure range. *Physics of the Earth and Planetary Interiors,* 174: 181-91.

Ballhaus, C., Berry, R.F and Green, D.H., (1990). Oxygen fugacity controls in the Earth's upper mantle. *Nature,* 348: 437-40.

Bastin, G.F. and Heijligers, H.J.M., (1986). Quantitative Electron Probe Microanalysis of Carbon in Binary Carbides. *X-ray Spectrometry,* 15: 135-41.

Campbell, A.J., Danielson, L., Righter, K., Seagle, C.T., Wang, Y. and Prakapenka, V.B., (2009). High pressure effects on the iron-iron oxide and nickel-nickel oxide oxygen fugacity buffers. *Earth and Planetary Science Letters,* 286(3-4): 556-64.

Chabot, N.L., Campbell, A.J., Mcdonough, W.F., Draper, D.S., Agee, C.B., Humayun, M., Watson, H.C., Cottrell, E., and Saslow, S.A., (2008). The Fe-C System at 5GPa and Implications for Earth's Core. *Geochimica Et Cosmochimica Acta*, 72: 4146-158.

Chipman, J., (1972). Thermodynamics and Phase Diagram of the Fe-C System. *Metallurgical Transactions*, 3: 55-64.

Dasgupta, R., Hirschmann, M.M., and Withers, A.W., (2004). Deep global cycling of carbon constrained by the solidus of anhydrous, carbonated eclogite under upper mantle conditions. *Earth and Planetary Science Letters,* 227: 73-85.

Dasgupta, R., and Walker, D,. (2008). Carbon Solubility in Core Melts in a Shallow Magma Ocean Environment and Distribution of Carbon between the Earth's Core and the Mantle. *Geochimica Et Cosmochimica Acta,* 72: 4627-641.

Dasgupta, R. and Hirschmann, M.M., (2010). The deep carbon cycle and melting in Earth's interior. *Earth and Planetary Science Letters (Frontiers),* 298: 1-13.

Fei, Y., Wang, Y. and Deng, L., (2007). Melting relations in the F-C-S system at high pressure: implications for the chemistry of the cores of the terrestrial planets. *Lunar and planetary science,* 38: 1231.

Frost, D.J., Liebske, C., Langenhorst, F., McCammon, C.A., Trønnes, R.G., and Rubie, D.C., (2004). Experimental evidence for the existence of iron-rich metal in the Earth's lower mantle. *Nature,* 428: 409-412.

Frost, D.J., and McCammon C.A., (2008). The Redox State of Earth's Mantle. *The Annual Review of Earth and Planetary Sciences,* 36: 389-420.

Goncharov, A.G., Ionov, D.A., Doucet, L.S. and Pokhilenko, L.N., (2012). Thermal state, oxygen fugacity and C–O–H fluid speciation in cratonic lithospheric mantle: New data on peridotite xenoliths from the Udachnaya kimberlite, Siberia. *Earth and Planetary Science Letters,* 357-358: 99-110.

Hirschmann, M.M., and Dasgupta, R., (2009). The H/C ratios of Earth's near-surface and deep reservoirs, and consequences for deep Earth volatile cycles. *Chemical Geology,* 262: 4-16.

Hirschmann, M.M., and Ghiorso, M.S., (1994). Activities of nickel, cobalt, and manganese silicates in magmatic liquids and applications to olivine/liquid and to silicate/metal partitioning. *Geochimica et Cosmochimica Acta,* 58, 4109-126.

Holzheid, A., and Grove, T.L., (2005). The effect of metal composition on Fe-Ni partition behavior between olivine and FeNi-metal, FeNi-carbide, FeNi-sulfide at elevated pressure. *Chemical Geology*, 221: 207-24.

Jacob, D.E., Kronz, A., and Viljoen, K.S., (2004) Cohenite, native iron and troilite inclusions in garnets from polycrystalline diamond aggregates. *Contributions to Mineral Petrology*, 146: 566-76.

Kaminsky, Felix V., and Wirth, Richard, (2011) Iron Carbide Inclusions in Lower-Mantle Diamond from Juina, Brazil. *The Canadian Mineralogist*, 49: 555-72.

Lord, O.T., Walter, M.J., Dasgupta, R., Walker, D., and Clark, S.M., (2009). Melting in the Fe–C System to 70 GPa. *Earth and Planetary Science Letters*, 284: 157-67.

McCammon, C. A., (2005). The paradox of mantle redox. *Science*, 308: 807-08.

Nakajima, Y., Takahashi, E., Toshihiro, S., and Funakoshi K., (2009). "Carbon in the Core" Revisited. *Physics of the Earth and Planetary Interiors*, 174: 202-11.

O'Neill, H.S.C., McCammon, C.A., Canil, D., Rubie, D.C., Ross II, C.R., and Seifert, F., (1993). Mössbauer spectroscopy of mantle transition zone phases and determination of minimum Fe3+ content. *American Mineralogist (Letters)*, 78: 456-60.

Robaut, F., Crisci, A., Durand-Charre, M., and Jouanne, D., (2006). Practical aspects of carbon content determination in carburized steels by EPMA. *Microscopy and Microanalysis*, 12: 331-34.

Rohrbach, A., Ballhaus, C., Golla–Schindler, U., Ulmer, P., Kamenetsky V.S., and Kuzmin, D.V., (2007). Metal saturation in the upper mantle. *Nature*, 449: 456-58.

Rohrbach, A., Ballhaus, C., Ulmer, P., Golla–Schindler, U., and Schonbohm, D., (2011). Experimental Evidence for a Reduced Metal-saturated Upper Mantle. *Journal of Petrology,* 52: 717-31.

Romig, Jr., A.D., and Goldstein, J.I., (1978). Determination of the Fe-Rich Portion of the Fe-Ni-C Phase Diagram. *Metallurgical Transactions A,* 9A: 1599-1609.

Seifert, S., O'Neill, H.S.C., and Brey, G., (1988). The partitioning of Fe, Ni and Co between olivine, metal, and basaltic liquid: An experimental and thermodynamic investigation, with application to the composition of the lunar core. *Geochimica Et Cosmochimica Acta,* 52: 603-16.

Sleep N.H., and Zahnle, K., (2001). Carbon dioxide cycling and implications for climate on ancient Earth. *Journal of Geophysical Research,* 106: 1373-399.

Stachel, Thomas., (2001). Diamonds from the asthenosphere and the transition zone. *European Journal of Minerals,* 13: 883-92.

Stagno, V., and Frost, D.J., (2010). Carbon speciation in the asthenosphere: Experimental measurements of the redox conditions at which carbonate-bearing melts coexist with graphite or diamond in peridotite assemblages. *Earth and Planetary Science Letters,* 300: 72-84.

Stewart, A.J., (2006). Planetary cores: effect and behaviour of minor elements on the Fe-S system to 40 GPa. Unpub. Ph.D. thesis ETH, Zürich.

Stixrude, Lars and Lithgow-Bertelloni, Carolina. (2007) Influence of phase transformations on lateral heterogeneity and dynamics in Earth's mantle. *Earth and Planetary Science Letters,* 263: 45-55.

Strong H.M., and Chrenko, R.M., (1971). Further Studies on Diamond growth rates and physical properties of laboratory-made diamond. *The Journal of Physical Chemistry,* 75: 1838-843.

Strong, H.M., and Hanneman, R.E., (1967). Crystallization of Diamond and Graphite. *The Journal of Chemical Physics,* 46: 3668-676.

Tappert, Ralf., Stachel, Thomas., Harris, Jeff W., Muehlenbachs, Karlis., Ludwig, Thomas., and Brey, Gerhard P., (2005). Subducting oceanic crust: The source of deep diamonds. *Geology,* 33: 565-68.

Taylor, W.R., and Green, D.H., (1987). The petrogenetic role of methane: effect on liquidus phase relations and the solubility mechanism of reduced C-H volatiles. *In Magmatic processes: physicochemical principles,* Vol. 1 (ed. B.O. Mysen) pp. 121-37.

Walter, M.J., Bulanova1, G.P., Armstrong, L.S., Keshav, S., Blundy, J.D., Gudfinnsson, G., Lord, O.T., Lennie, A.R., Clark, S.M., Smith, C.B., and Gobbo, L., (2008). Primary carbonatite melt from deeply subducted oceanic crust. *Nature,* 454: 622-26.

Walter, M.J., Kohn, S.C., Araujo, D., Bulanova, G.P., Smith C.B., Gaillou, E., Wang, J., Steele, A. and Shirey S.B., (2011). Deep Mantle Cycling of Oceanic Crust: Evidence from Diamonds and Their Mineral Inclusions. *Science,* 7: 54-7.

Wood, B.J., (1993). Carbon in the core. *Earth and Planetary Science Letters,* 117: 593-607.

Xirouchakis, D., Hirschmann, M.M., and Simpson, J., (2001). The effect of titanium on the silica content and on mineral-liquid partitioning of mantle-equilibrated melts. *Geochimica et Cosmochimica Acta*, 65: 2029-045.

Appendix

Table 1. Compositions of all run products.

Experiment number	Pressure	Temperature	Run time	Capsule	Bulk Composition*	Phases Present	Ni (wt%)	Fe (wt%)	C (wt%)***	Sum (wt%)
A921	3 GPa	1000°C	24 Hours	Al_2O_3	Fe/(Fe+Ni)=0	Alloy + Graphite	99.68	0	0.8	100.48
A921	3 GPa	1000°C	24 Hours	Al_2O_3	Fe/(Fe+Ni)=1/7	Alloy + Graphite	87.01	13.36	0.31	100.68
A921	3 GPa	1000°C	24 Hours	Al_2O_3	Fe/(Fe+Ni)=2/7	Alloy + Graphite	72.17	27.52	0.38	100.07
A921	3 GPa	1000°C	24 Hours	Al_2O_3	Fe/(Fe+Ni)=3/7	Alloy + Graphite	59.46	40.06	0.32	99.84
A905	3 GPa	1000°C	24 Hours	Al_2O_3	Fe/(Fe+Ni)=4/7	Alloy + Graphite	43.96	56.03	0.6	100.59
A905	3 GPa	1000°C	24 Hours	Al_2O_3	Fe/(Fe+Ni)=5/7	Alloy + Graphite	28.96	70.06	0.66	99.68
A905 Alloy Composition	3 GPa	1000°C	24 Hours	Al_2O_3	Fe/(Fe+Ni)=6/7	Carbide + Alloy	15.37	82.99	1.63	99.99
A905 Alloy Composition	3 GPa	1000°C	24 Hours	Al_2O_3	Fe/(Fe+Ni)=1	Carbide + Alloy	0	98.12	2.24	100.36
A905 Carbide Composition	3 GPa	1000°C	24 Hours	Al_2O_3	Fe/(Fe+Ni)=6/7	Carbide + Alloy	9.9	83.62	6.24	99.76
A905 Carbide Composition	3 GPa	1000°C	24 Hours	Al_2O_3	Fe/(Fe+Ni)=1	Carbide + Alloy	0	93.28	6.63	99.91
A780	3 GPa	1250°C	24 Hours	Al_2O_3	Fe/(Fe+Ni)=0	Alloy + Graphite	99.59	0	0.88	100.47
A780	3 GPa	1250°C	24 Hours	Al_2O_3	Fe/(Fe+Ni)=1/7	Alloy + Graphite	86.62	13.44	0.31	100.37
A780	3 GPa	1250°C	24 Hours	Al_2O_3	Fe/(Fe+Ni)=2/7	Alloy + Graphite	73.02	26.90	0.28	100.2
A780	3 GPa	1250°C	24 Hours	Al_2O_3	Fe/(Fe+Ni)=3/7	Alloy + Graphite	57.50	41.5	0.39	99.39
A836	3 GPa	1250°C	24 Hours	Al_2O_3	Fe/(Fe+Ni)=4/7	Alloy + Graphite	43.06	56.89	0.83	100.78
A836	3 GPa	1250°C	24 Hours	Al_2O_3	Fe/(Fe+Ni)=5/7	Melt^	26.50	68.50	5.00	100
A836	3 GPa	1250°C	24 Hours	Al_2O_3	Fe/(Fe+Ni)=6/7	Melt^	17.20	77.70	5.10	100
A836	3 GPa	1250°C	24 Hours	Al_2O_3	Fe/(Fe+Ni)=1	Melt^	0.00	95.60	4.40	100
M552	5 GPa	1200°C	24 Hours	Al_2O_3	Fe/(Fe+Ni)=0	Alloy + Graphite	98.56	0	0.96	99.52
M552	5 GPa	1200°C	24 Hours	Al_2O_3	Fe/(Fe+Ni)=1/7	Alloy + Graphite	86.44	13.45	0.42	100.31
M552	5 GPa	1200°C	24 Hours	Al_2O_3	Fe/(Fe+Ni)=2/7	Alloy + Graphite	80.73	18.82	0.52	100.07
M552	5 GPa	1200°C	24 Hours	Al_2O_3	Fe/(Fe+Ni)=3/7	Alloy + Graphite	70.05	30.16	0.46	100.67
M564	5 GPa	1200°C	24 Hours	Al_2O_3	Fe/(Fe+Ni)=4/7	Alloy + Graphite	44.83	54.08	0.81	99.72
M564	5 GPa	1200°C	24 Hours	Al_2O_3	Fe/(Fe+Ni)=5/7	Melt^	27.75	67.54	4.71	100
M564	5 GPa	1200°C	24 Hours	Al_2O_3	Fe/(Fe+Ni)=6/7	Melt^	14.74	80.59	4.67	100
M564	5 GPa	1200°C	24 Hours	Al_2O_3	Fe/(Fe+Ni)=1	Carbide + Graphite**	0	94.06	6.68	100.74
M565	5 GPa	1400°C	24 Hours	Al_2O_3	Fe/(Fe+Ni)=0	Melt^	97.05	0.00	2.95	100
M565	5 GPa	1400°C	24 Hours	Al_2O_3	Fe/(Fe+Ni)=1/7	Melt^	83.83	11.36	4.81	100
M565	5 GPa	1400°C	24 Hours	Al_2O_3	Fe/(Fe+Ni)=2/7	Melt^	73.01	23.44	3.55	100
M565	5 GPa	1400°C	24 Hours	Al_2O_3	Fe/(Fe+Ni)=3/7	Melt^	60.23	35.19	4.58	100
M547	5 GPa	1400°C	24 Hours	Al_2O_3	Fe/(Fe+Ni)=4/7	Melt^	42.90	53.60	3.50	100
M547	5 GPa	1400°C	24 Hours	Al_2O_3	Fe/(Fe+Ni)=5/7	Melt^	29.60	65.80	4.60	100
M547	5 GPa	1400°C	24 Hours	Al_2O_3	Fe/(Fe+Ni)=6/7	Melt^	14.30	80.65	5.05	100
M547	5 GPa	1400°C	24 Hours	Al_2O_3	Fe/(Fe+Ni)=1	Melt^	0.00	95.00	5.00	100
M568	7 GPa	1200°C	24 Hours	Al_2O_3	Fe/(Fe+Ni)=0	Alloy + Graphite	98.5	0	0.80	99.3
M568	7 GPa	1200°C	24 Hours	Al_2O_3	Fe/(Fe+Ni)=1/7	Alloy + Graphite	86	13	0.30	99.3
M568	7 GPa	1200°C	24 Hours	Al_2O_3	Fe/(Fe+Ni)=2/7	Alloy + Graphite	74.5	24.84	0.34	99.68
M568	7 GPa	1200°C	24 Hours	Al_2O_3	Fe/(Fe+Ni)=3/7	Alloy + Graphite	61.5	38.8	0.40	100.7
M571	7 GPa	1200°C	24 Hours	Al_2O_3	Fe/(Fe+Ni)=4/7	Alloy + Graphite	46.26	53.08	0.80	100.14
M571	7 GPa	1200°C	24 Hours	Al_2O_3	Fe/(Fe+Ni)=5/7	Carbide + Graphite**	17.54	78.09	6.29	101.92
M571	7 GPa	1200°C	24 Hours	Al_2O_3	Fe/(Fe+Ni)=6/7	Carbide + Graphite**	14.71	80.93	6.11	101.75
M571	7 GPa	1200°C	24 Hours	Al_2O_3	Fe/(Fe+Ni)=1	Carbide + Graphite**	0	95.21	6.5	101.71
M590	7 GPa	1200°C	24 Hours	Al_2O_3	Fe/(Fe+Ni)=5/7	Alloy + Graphite	27.56	72.33	0.63	100.52
M590	7 GPa	1200°C	24 Hours	Al_2O_3	Fe/(Fe+Ni)=6/7	Melt^	14.37	80.31	5.32	100
M579	7 GPa	1400°C	24 Hours	Al_2O_3	Fe/(Fe+Ni)=1/7	Melt^	84.56	11.01	4.43	100
M579	7 GPa	1400°C	24 Hours	Al_2O_3	Fe/(Fe+Ni)=3/7	Melt^	51.08	43.75	5.17	100
M578	7 GPa	1400°C	24 Hours	Al_2O_3	Fe/(Fe+Ni)=4/7	Melt^	42.65	53.85	3.50	100
M578	7 GPa	1400°C	24 Hours	Al_2O_3	Fe/(Fe+Ni)=5/7	Melt^	29.60	66.00	4.40	100
M578	7 GPa	1400°C	24 Hours	Al_2O_3	Fe/(Fe+Ni)=1	Melt^	0.00	95.10	4.90	100

All bulk analysis has 5 wt% C
** More than 5 wt% C
*** Blank Corrected
^ Normalized

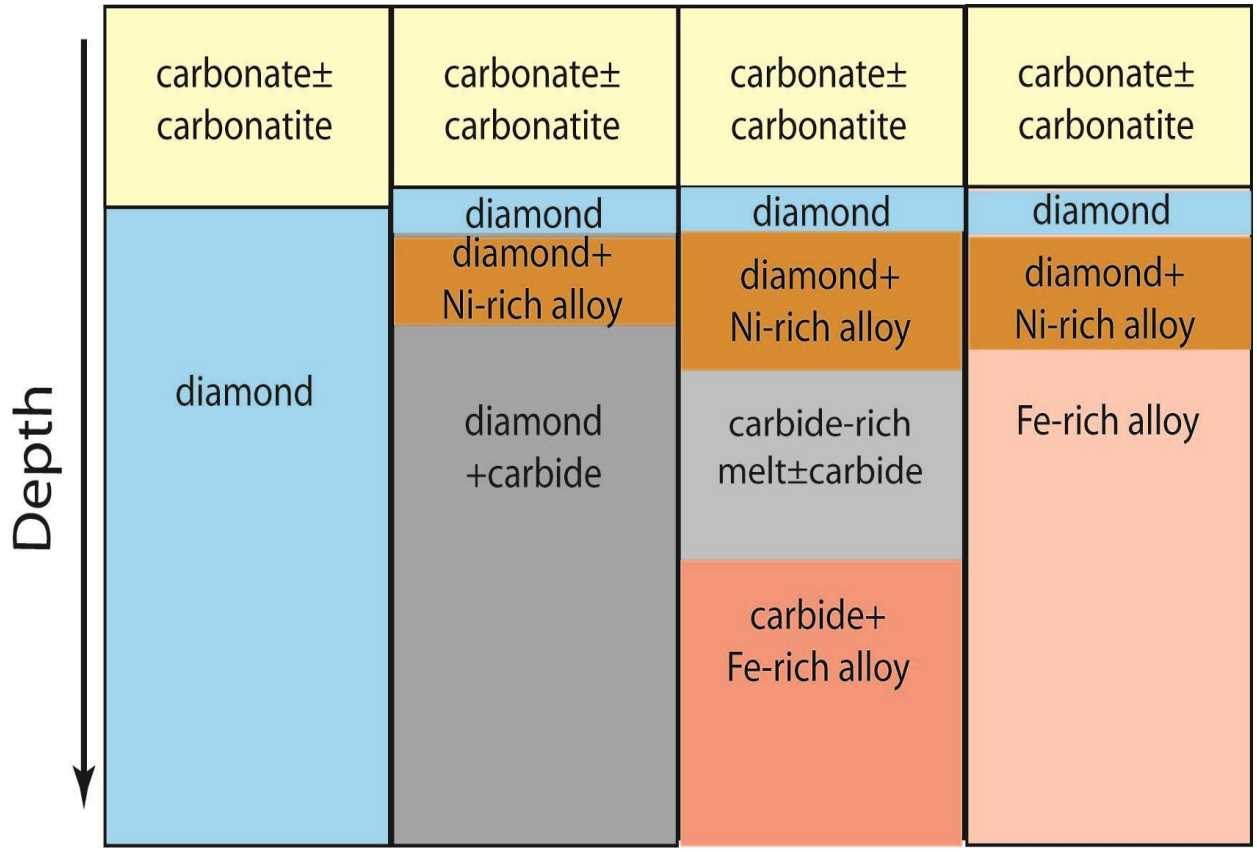

Figure 1. Different possible scenarios of principal carbon phases in the mantle with depth. Other possibilities are plausible, and there would be intervals of 3-phase stability (e.g., diamond +carbide +Ni-rich alloy) between 2 phase regions.

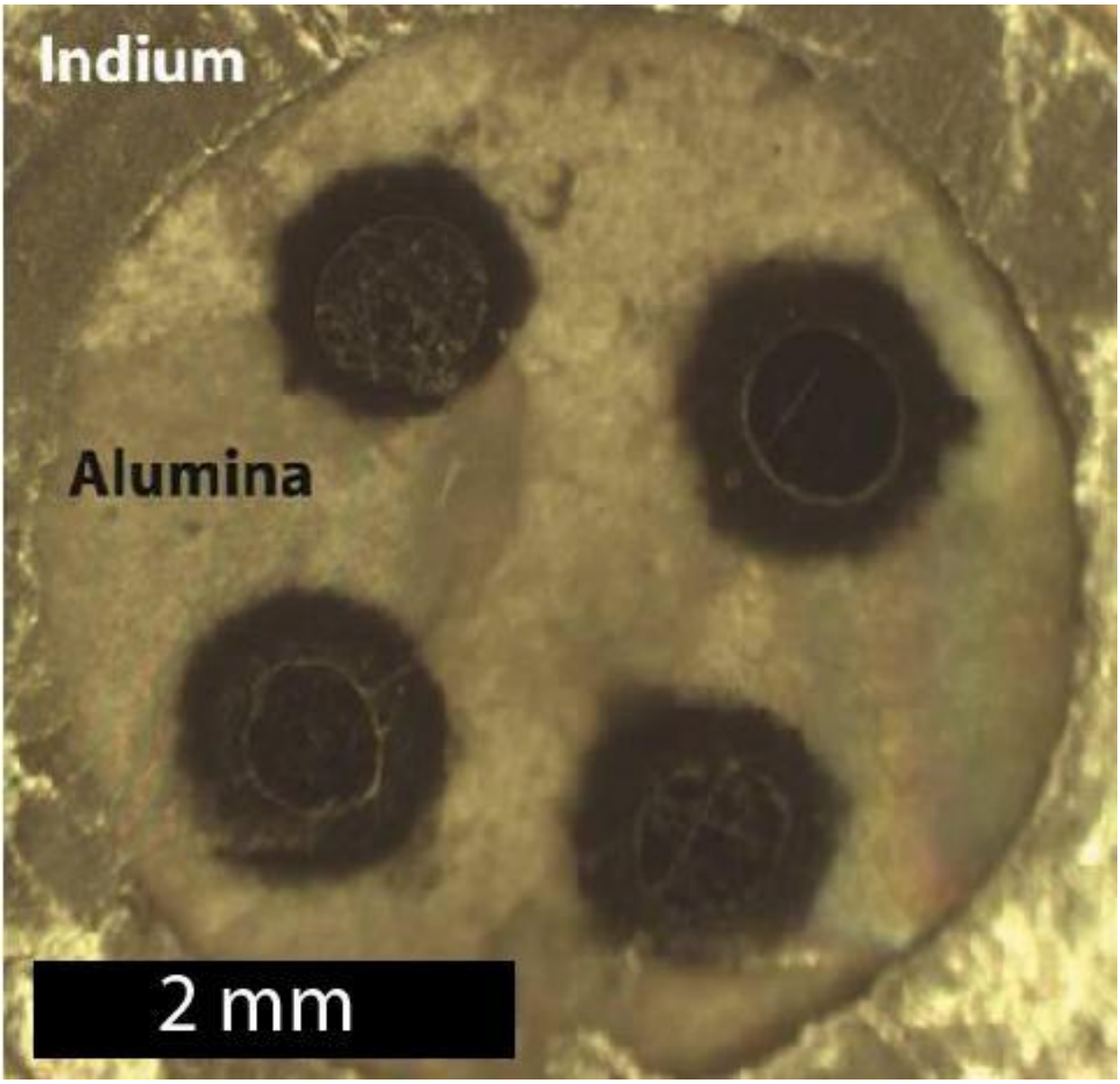

Figure 2. Optical image of multicapsule from piston cylinder experiment A780. The multicapsule consists of a 4-bore alumina thermocouple insulator. Each hole is filled with a different Fe-Ni-C composition. Diameter of alumina multicapsule is ~3.5 mm; each hole is 0.5 mm in diameter and 1.7 mm deep. Multicapsules from multi anvil experiments have a diameter of 1.7 mm and 1mm deep, while each hole is ~ 0.3 mm

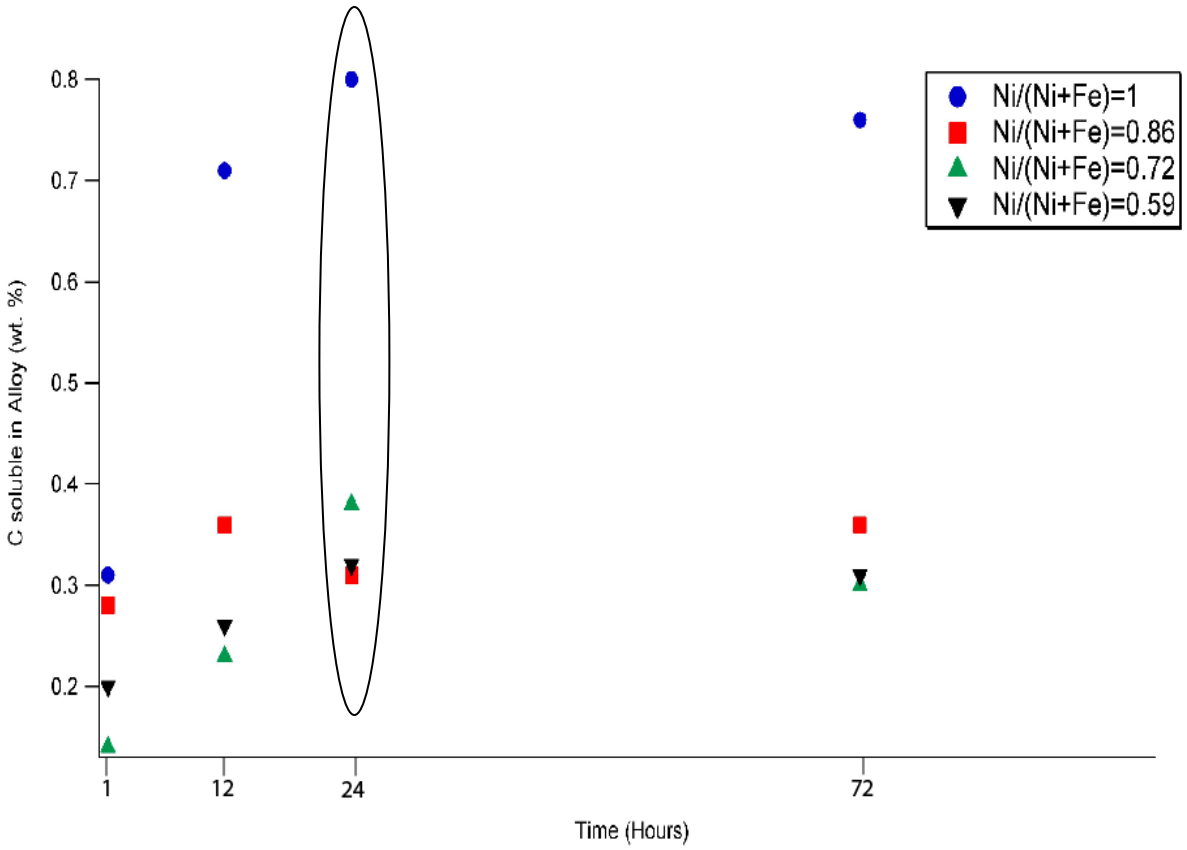

Figure 3. Carbon soluble in Ni-rich alloy experiments vs a time series at 1, 12, 24, and 72 hours. Corresponding textures and quantitative analysis determined that a 24 hour experiment was adequate.

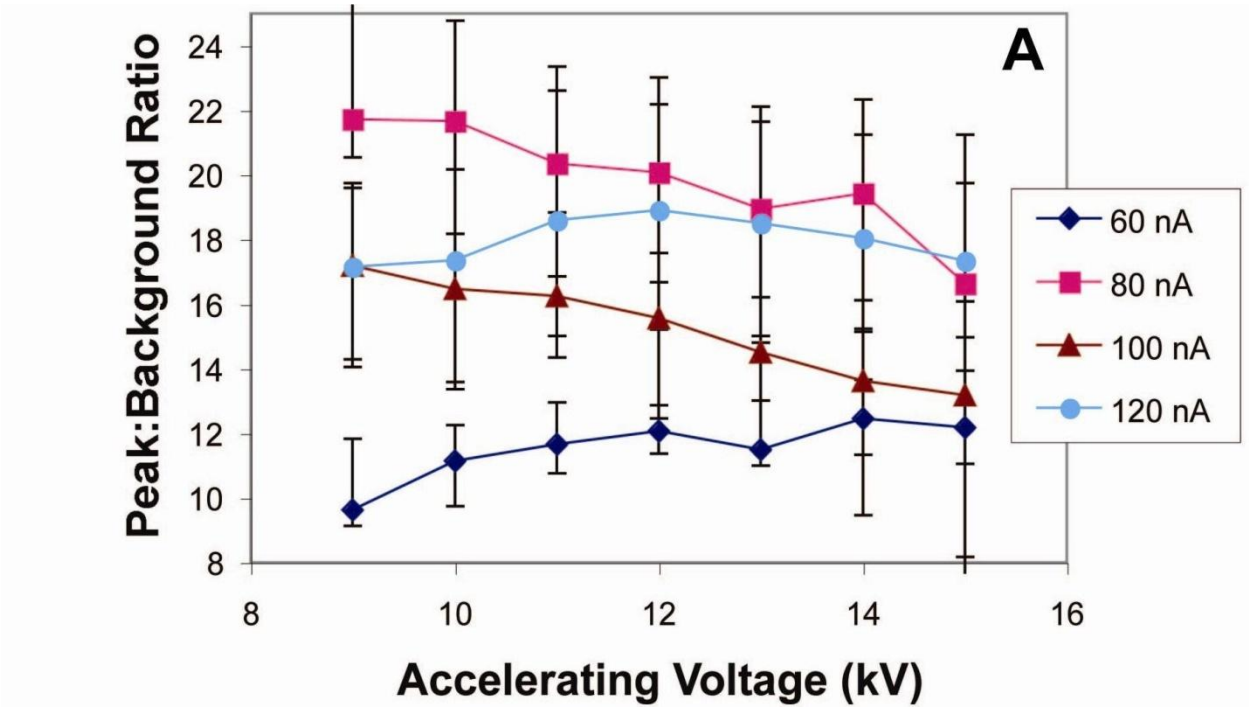

Figure 4. Analytical conditions for C using the UMN JEOL-JXA 8900 optimization for determined signal to background ratio for C Ka count using a multi-layer crystal (LDE2) of d = 9.7. Peak/background (*p/b*) for the C peak whilst analyzing the synthesized Fe3C standard gives optimal values at approximately 9-12 kV and 80 nA.

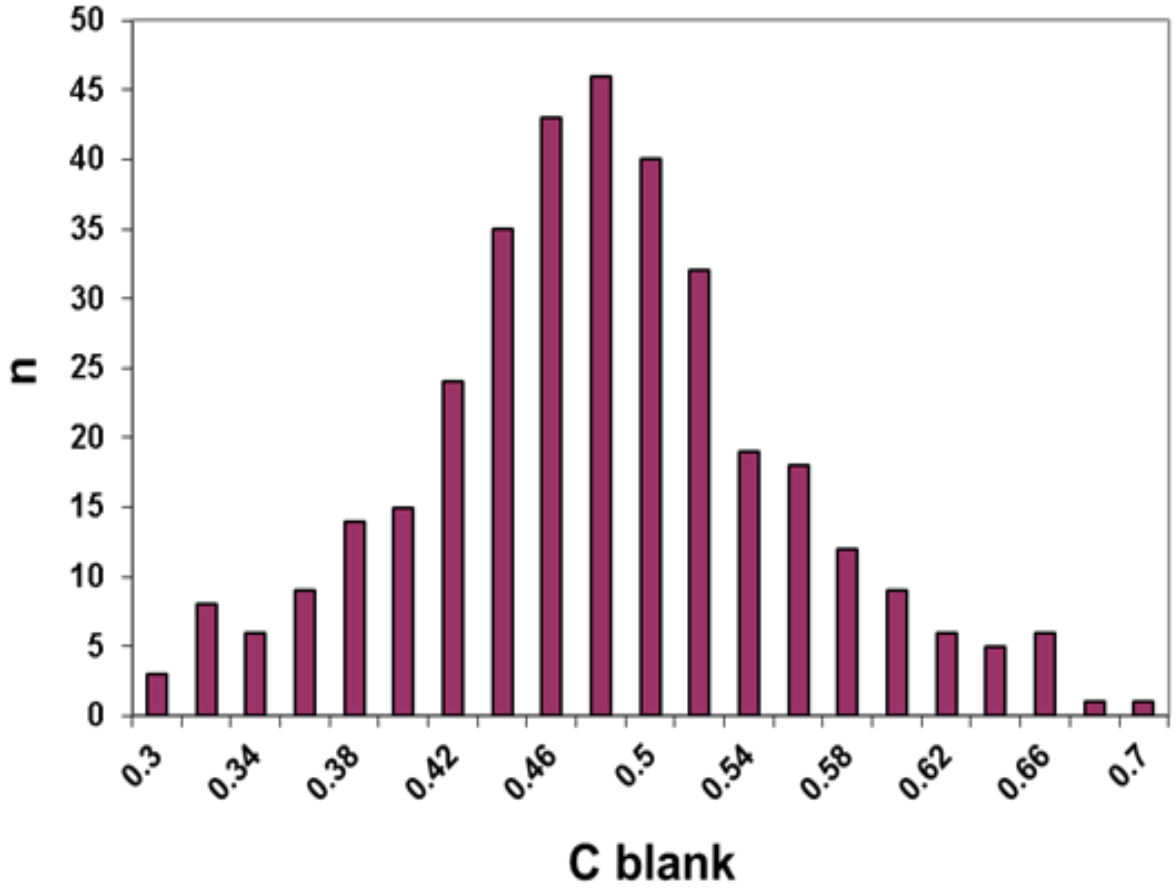

Figure 5. A histogram of analyses of carbon on a pure Fe standard (Fe 99.995 wt.%) of 352 analysis. our sessions revealed a persistent carbon contamination of 0.48±0.08 wt.% (1 standard deviation).

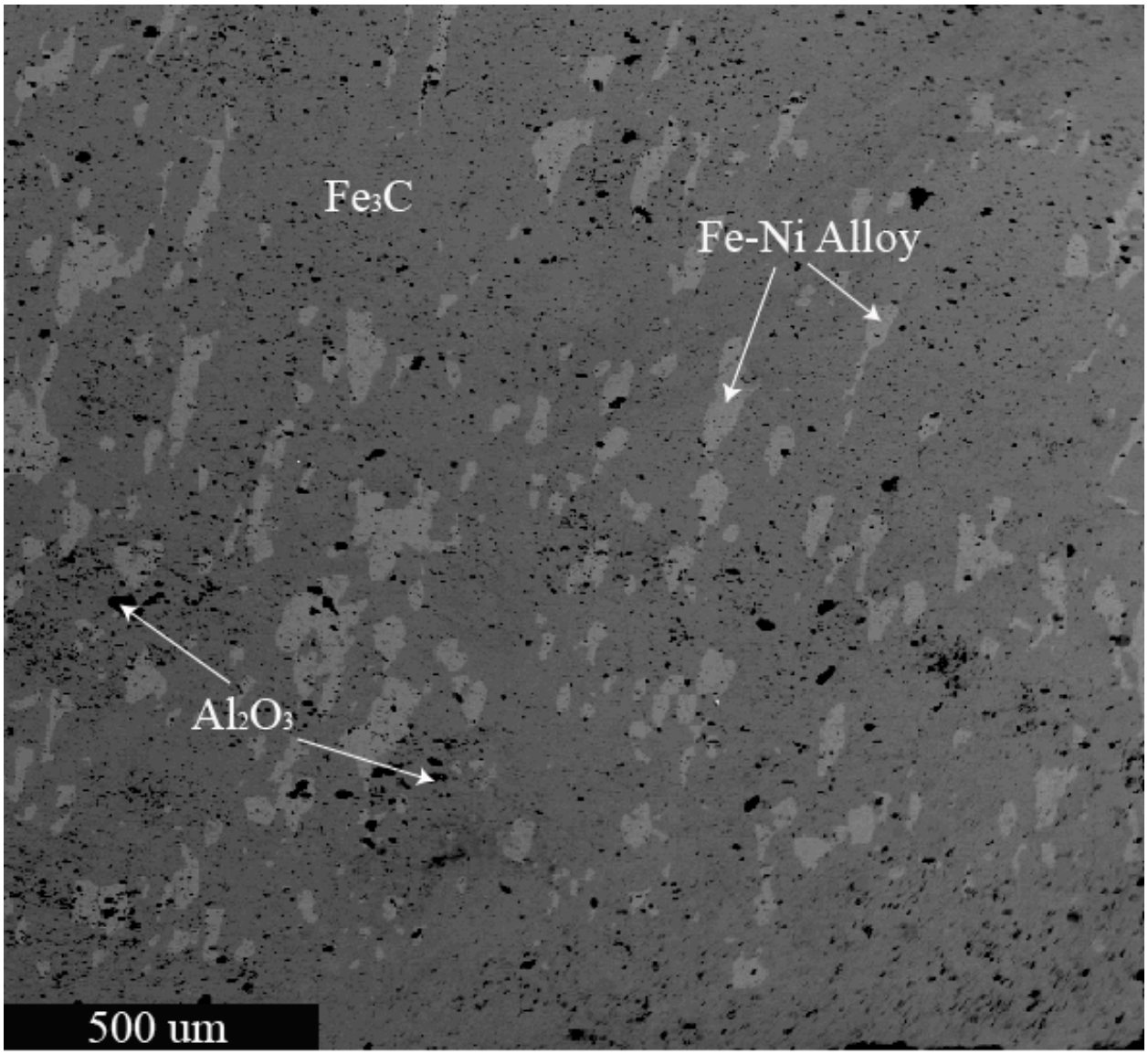

Figure 6. Backscattered electron image of a quenched Fe-Ni-C alloy from the experiment A905 (3 GPa, 1000°C) Ni/(Fe+Ni)=1/7. The quench phases comprise Fe-Ni alloy (lt. gray) and Fe_3C (gray). Black areas are Al_2O_3 from polishing of the capsule.

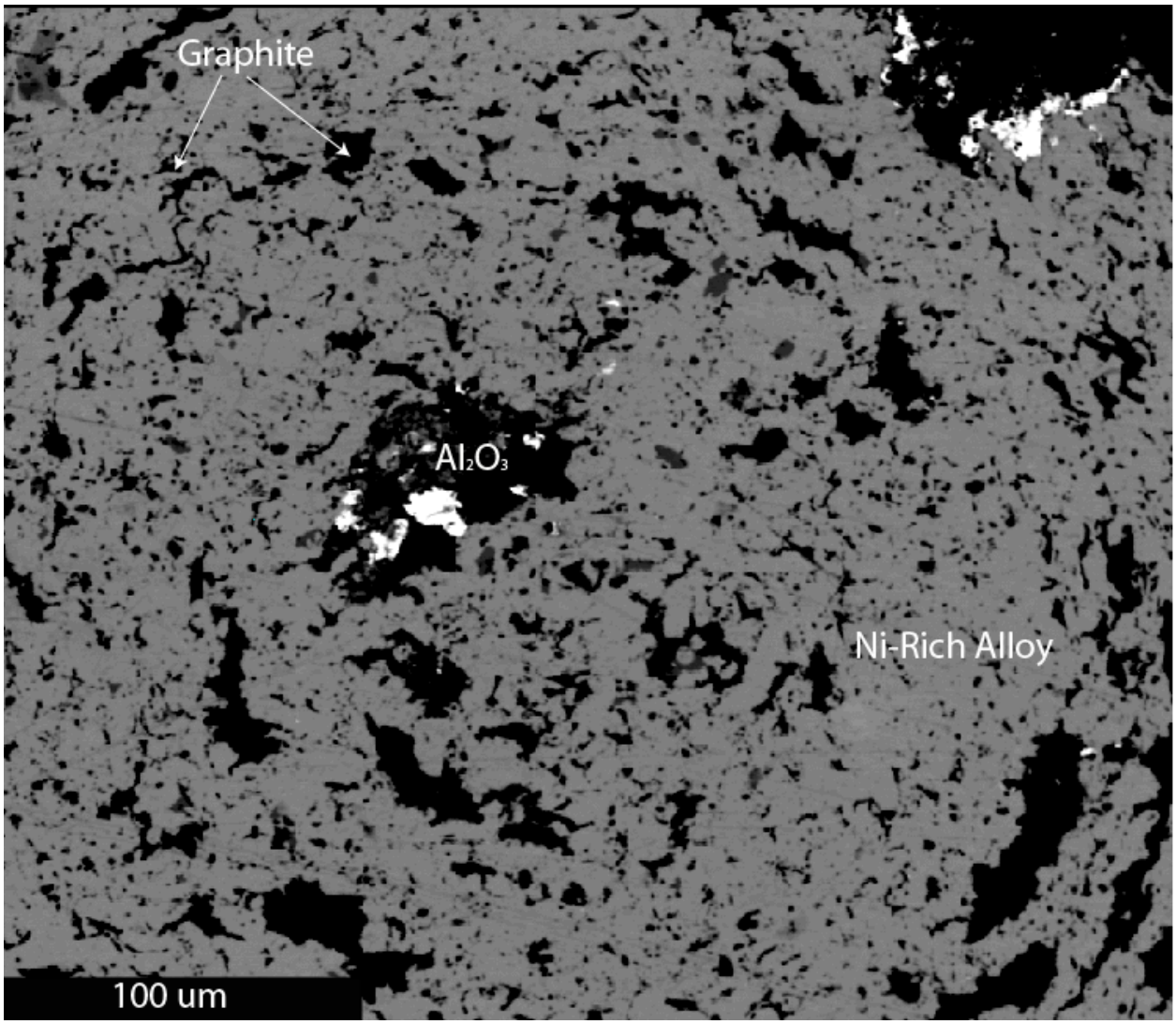

Figure 7. Backscattered electron image of a quenched Fe-Ni-C alloy from the experiment A780 (3 GPa, 1000°C) Ni/(Fe+Ni)=5/7. The quench phases comprise Fe-Ni alloy (gray) and graphite (Black). Black areas of graphite and Al_2O_3 from polishing of the capsule were distinguished by EDS.

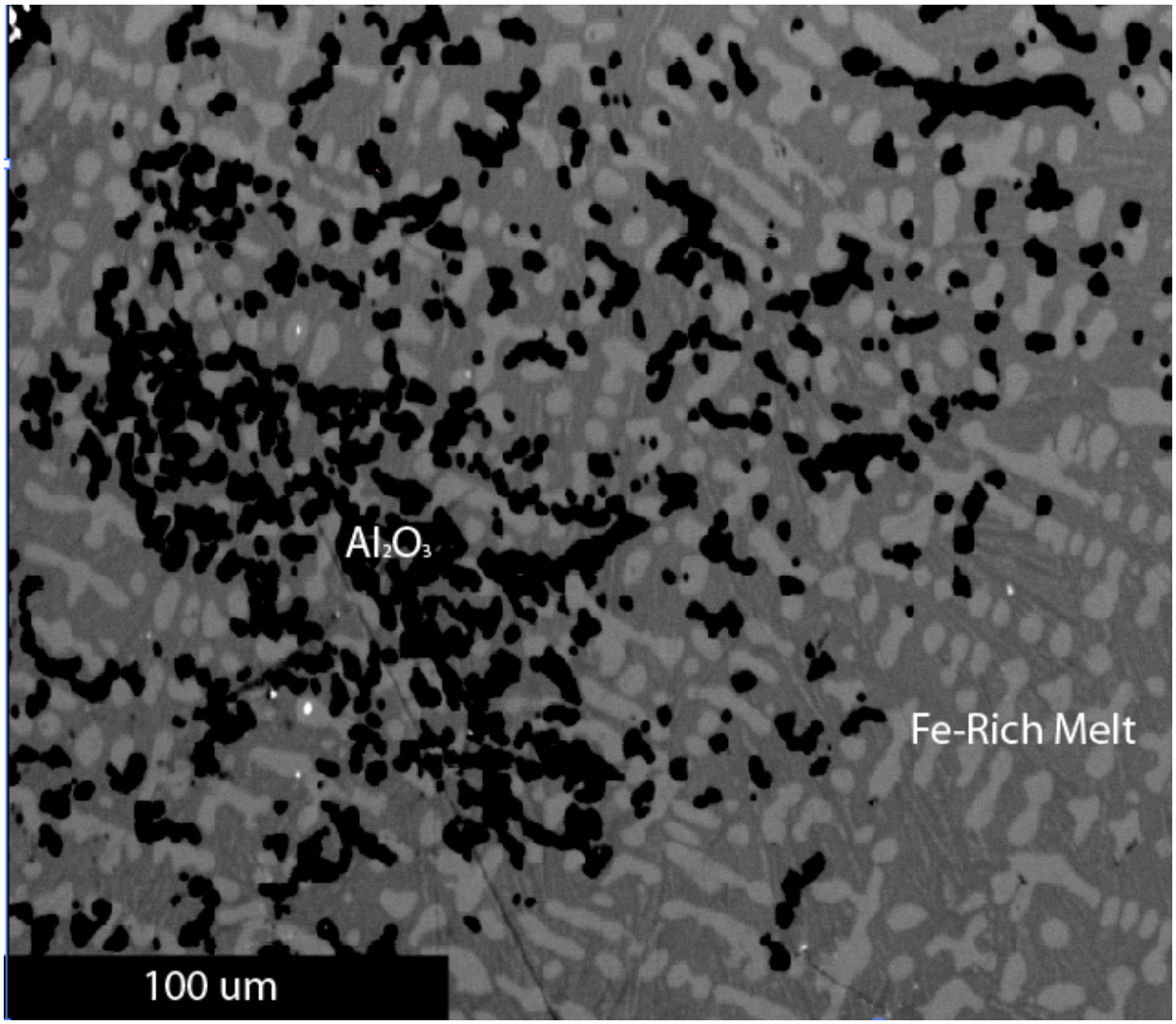

Figure 8. Backscattered electron image of a quenched Fe-Ni-C melt from the experiment A836 (3 GPa, 1250°C) Ni/(Fe+Ni)=1/7. The quench phases comprise Fe-Ni melt (gray dendrite texture). Black areas are Al_2O_3 from polishing of the capsule.

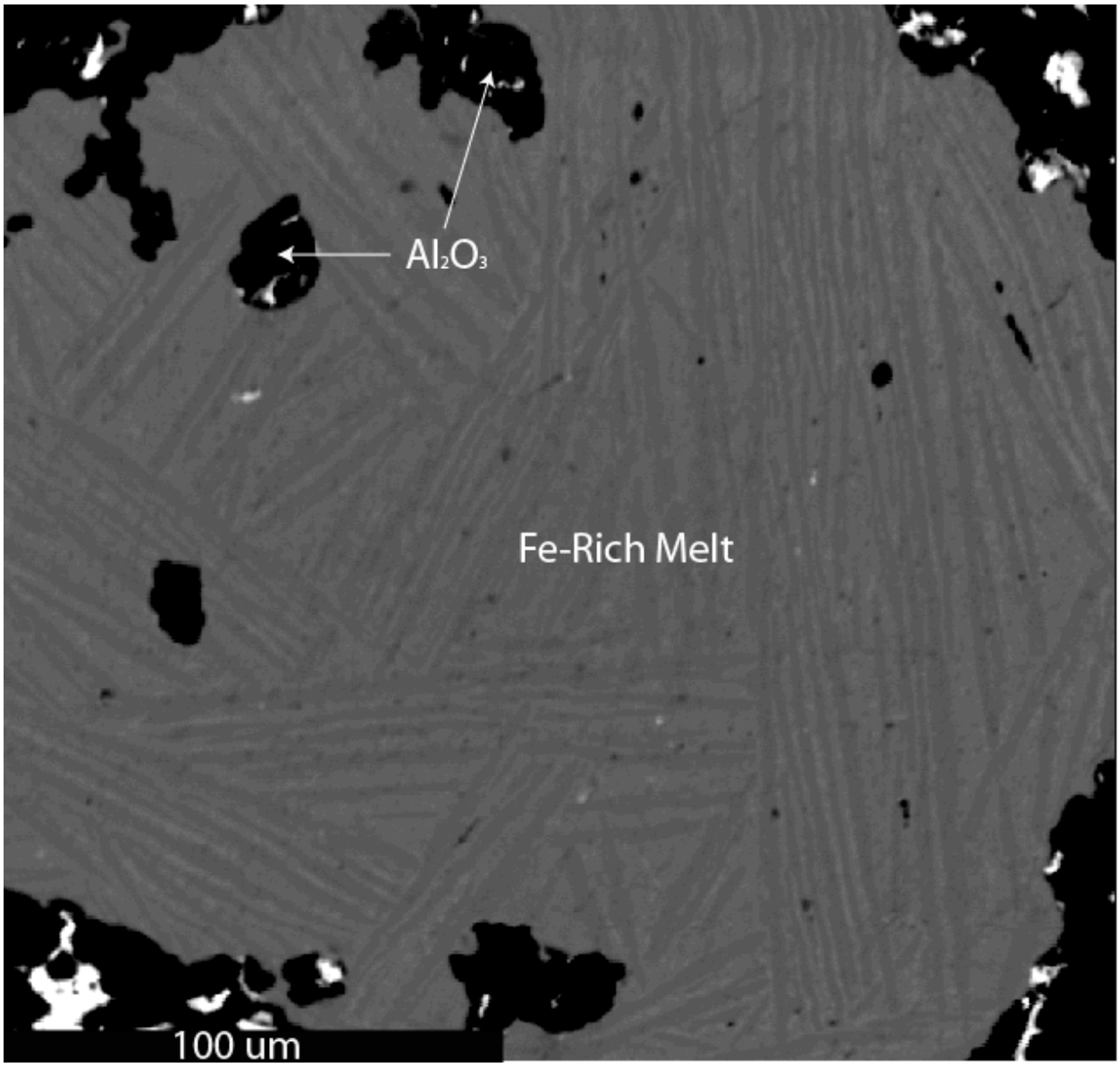

Figure 9. Backscattered electron image of a quenched Fe-C melt from the experiment M547 (5 GPa, 1400°C) Ni/(Fe+Ni)=0. The quench phases comprise Fe-Ni melt (gray acicular texture). Black areas are Al_2O_3 from polishing of the capsule.

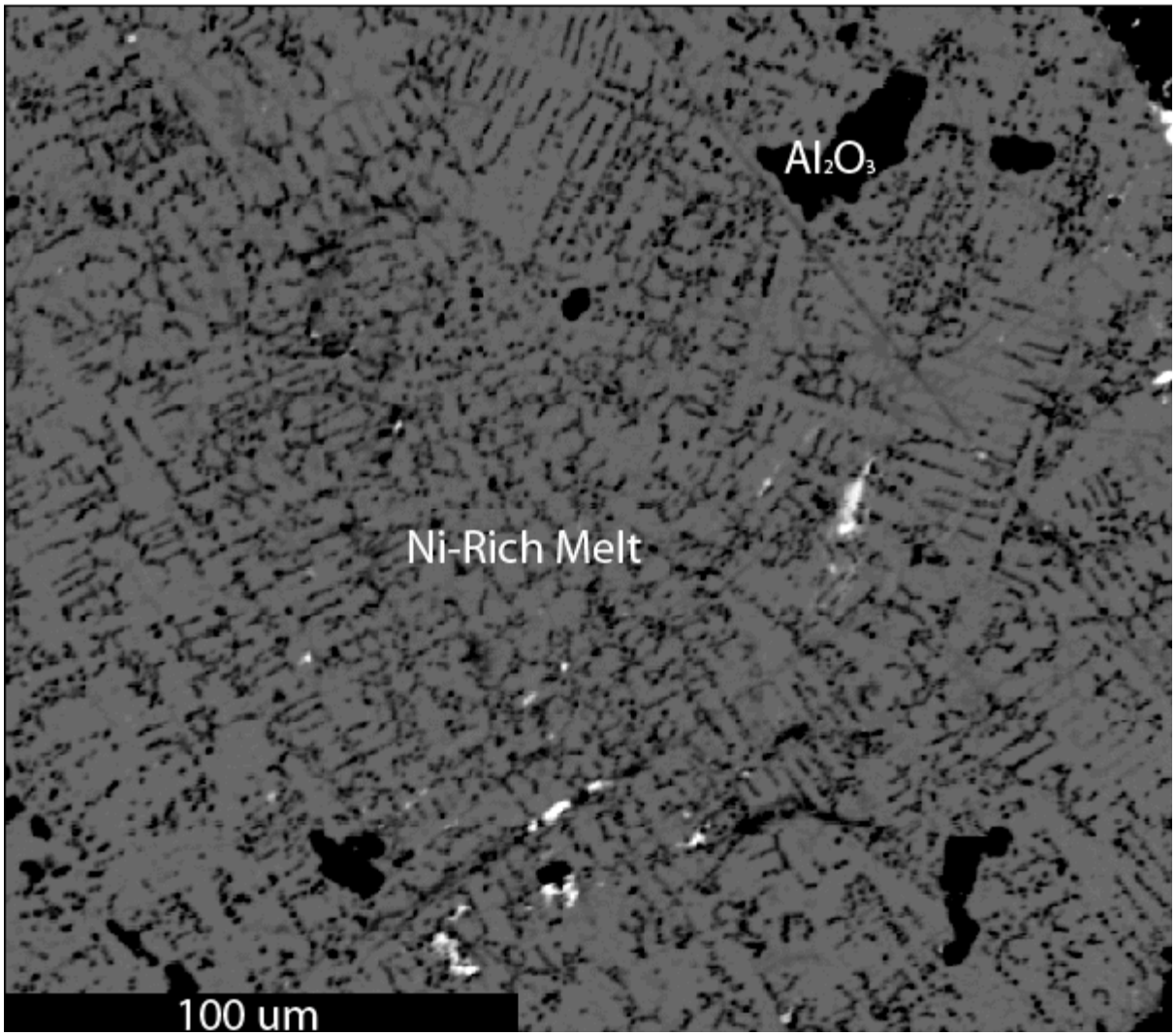

Figure 10. Backscattered electron image of a quenched Fe-Ni-C melt from the experiment M565 (5 GPa, 1400°C) Ni/(Fe+Ni)=5/7. The quench phases comprise Fe-Ni melt (gray gobular texture) and graphite (black). Black areas are Al_2O_3 from polishing of the capsule. Black areas of graphite and Al_2O_3 from polishing of the capsule were distinguished by EDS.

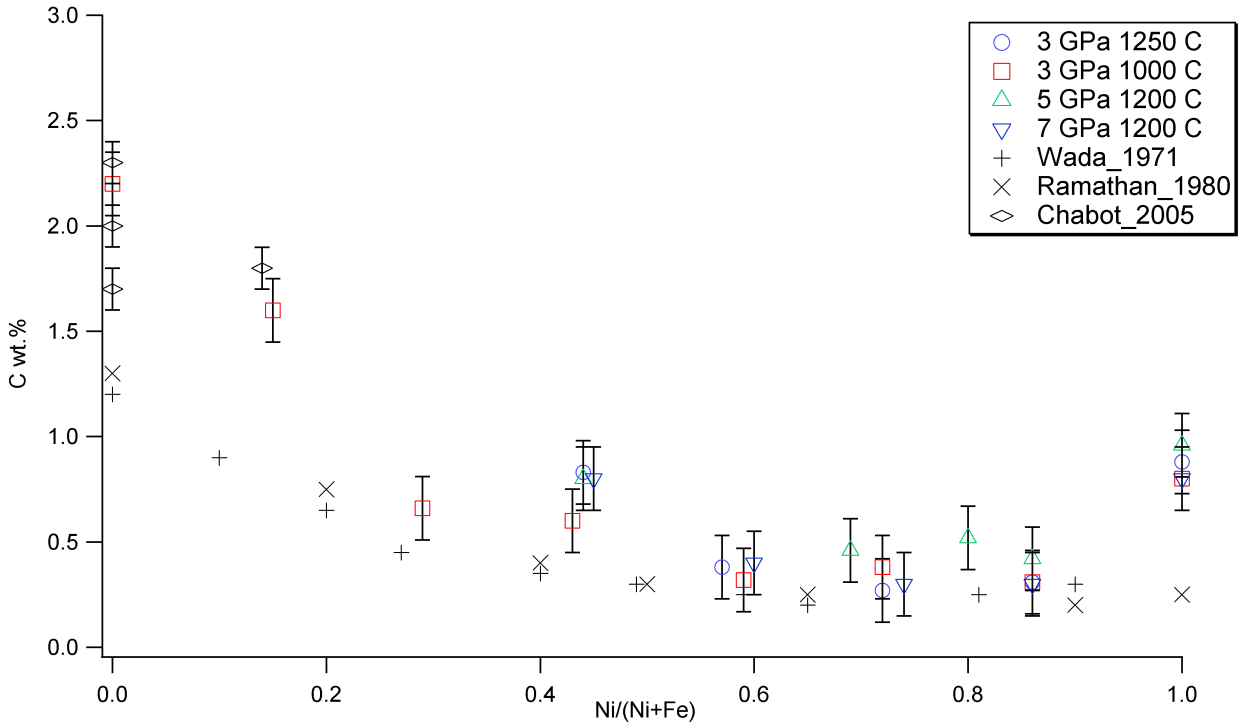

Figure 11. The solubility of C in solid Fe-Ni alloy as a function of changing Fe/Ni ratios. Blue circles, red squares, green triangles and dark blue upside down triangles are experimental results from this study. Black plus and X's are 1 atm experiments done by Wada and Ramathan. Black sideways diamonds are 5 GPa experiments done by Chabot et al.

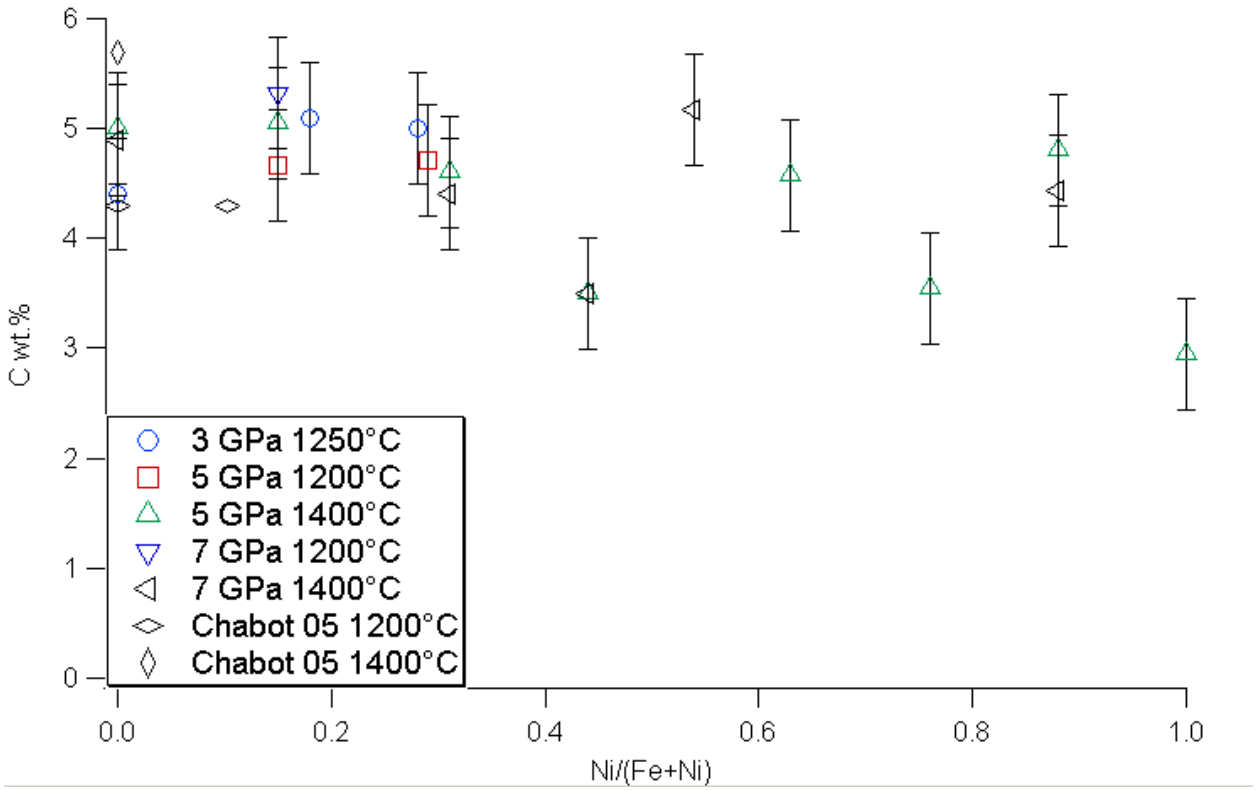

Figure 12. The solubility and the amount of C dissolved in Fe-Ni melt as a function of changing Fe/Ni ratios. Blue circles, red squares, green triangles, dark blue upside down triangles and black sideways black triangles are experimental results from this study. Black diamonds are 5 GPa experiments done by Chabot et al.

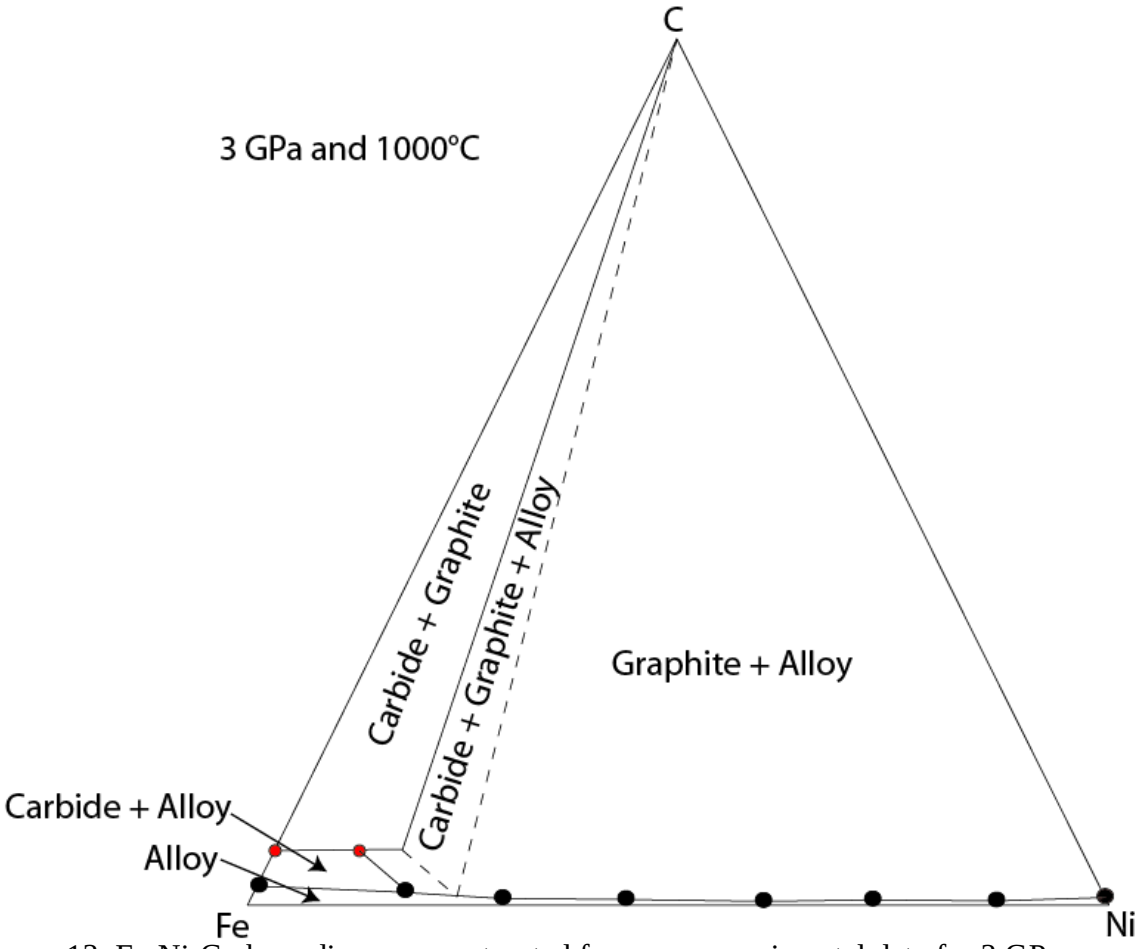

Figure 13. Fe-Ni-C phase diagram constructed from our experimental data for 3 GPa and 1000°C

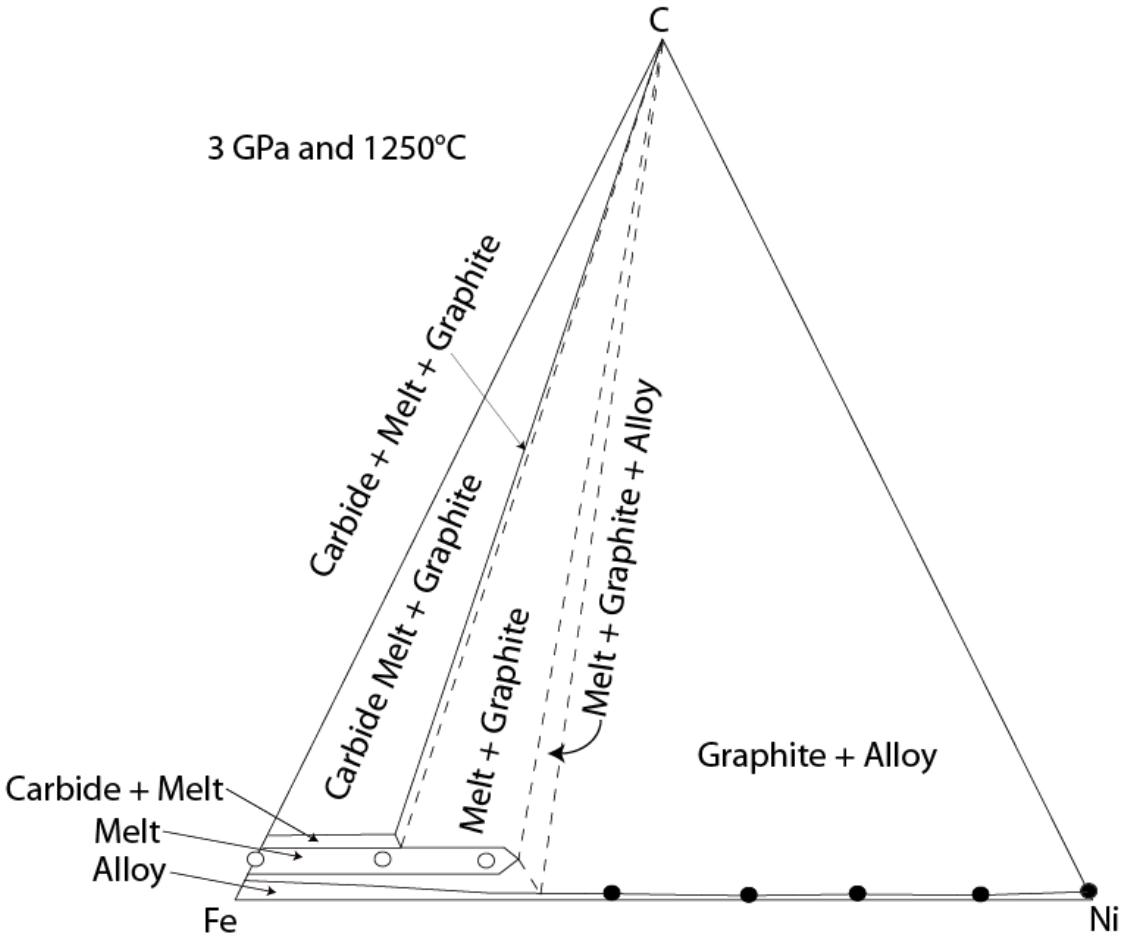

Figure 14. Fe-Ni-C phase diagram constructed from our experimental data for 3 GPa and 1250°C

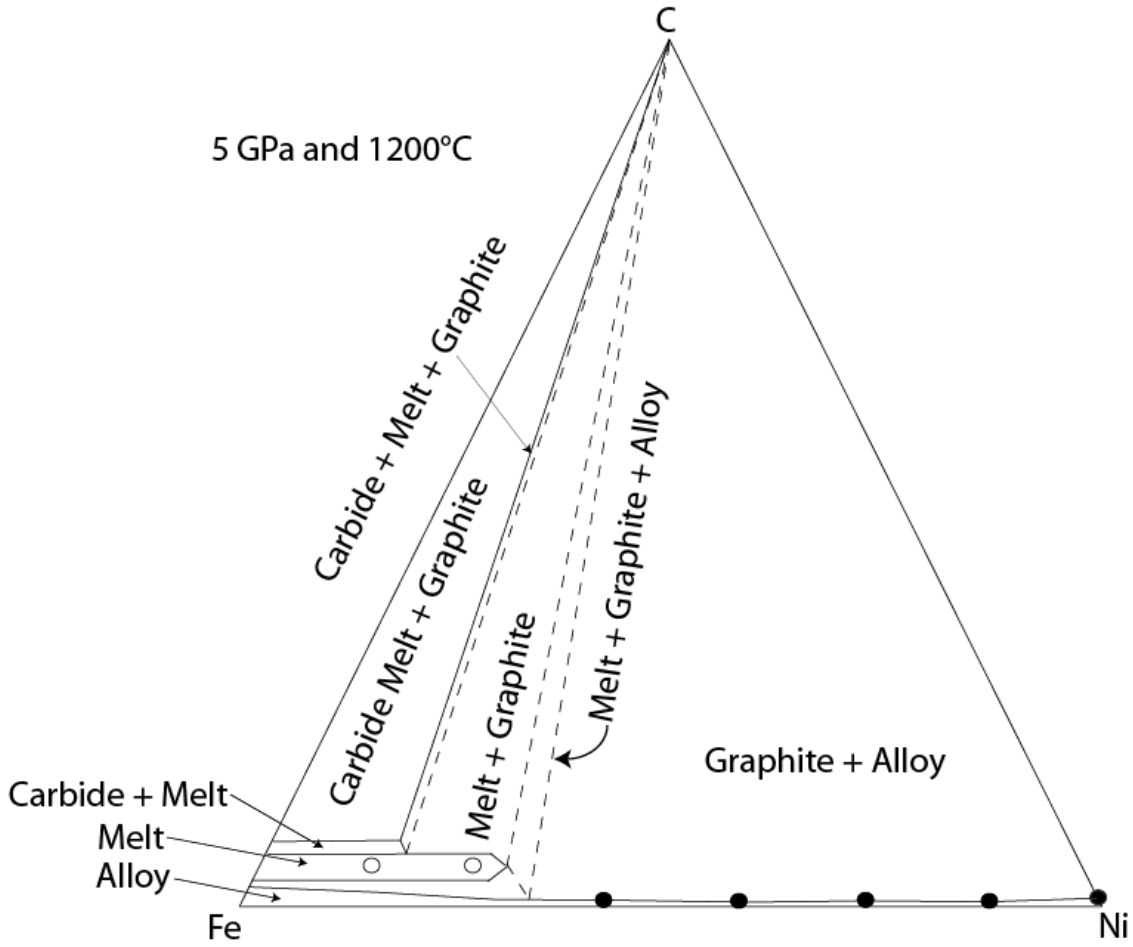

Figure 15. Fe-Ni-C phase diagram constructed from our experimental data for 5 GPa and 1200°C

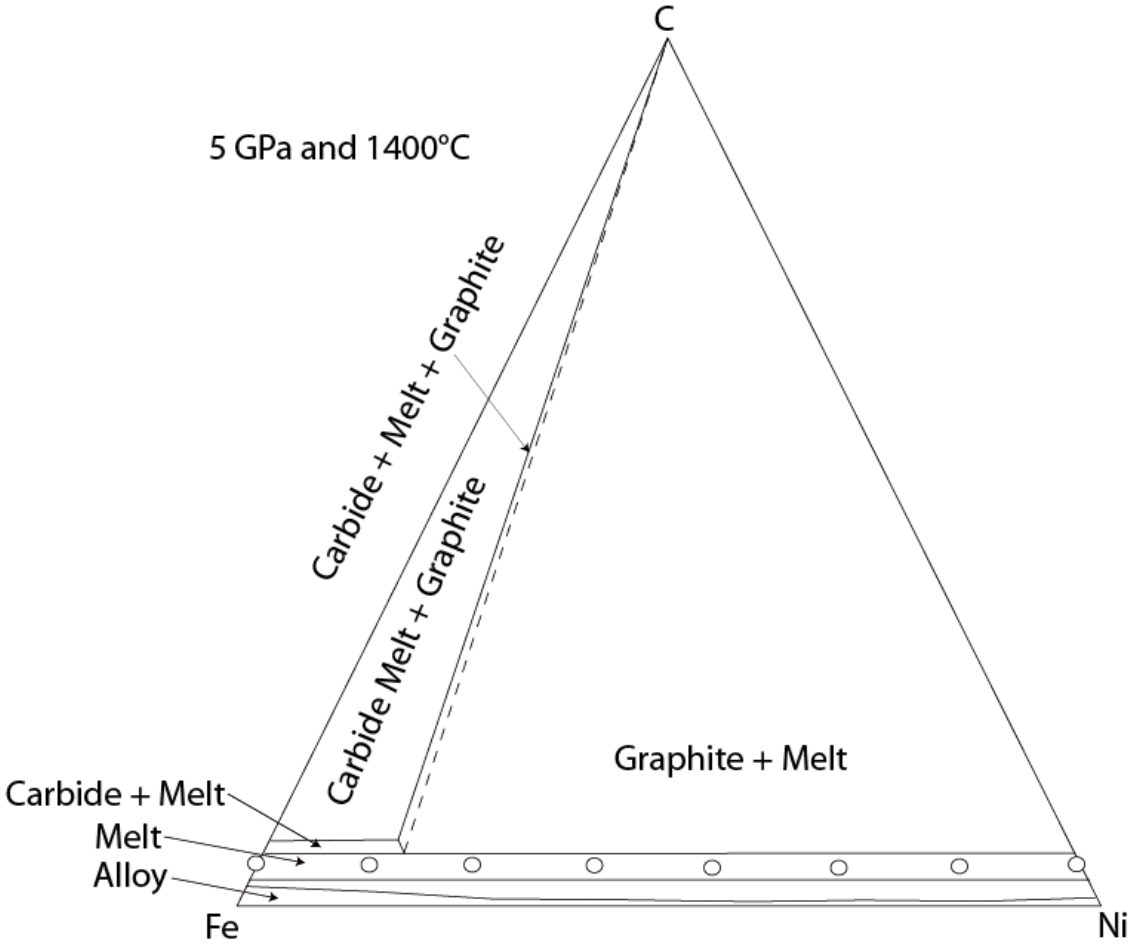

Figure 16. Fe-Ni-C phase diagram constructed from our experimental data for 5 GPa and 1400°C

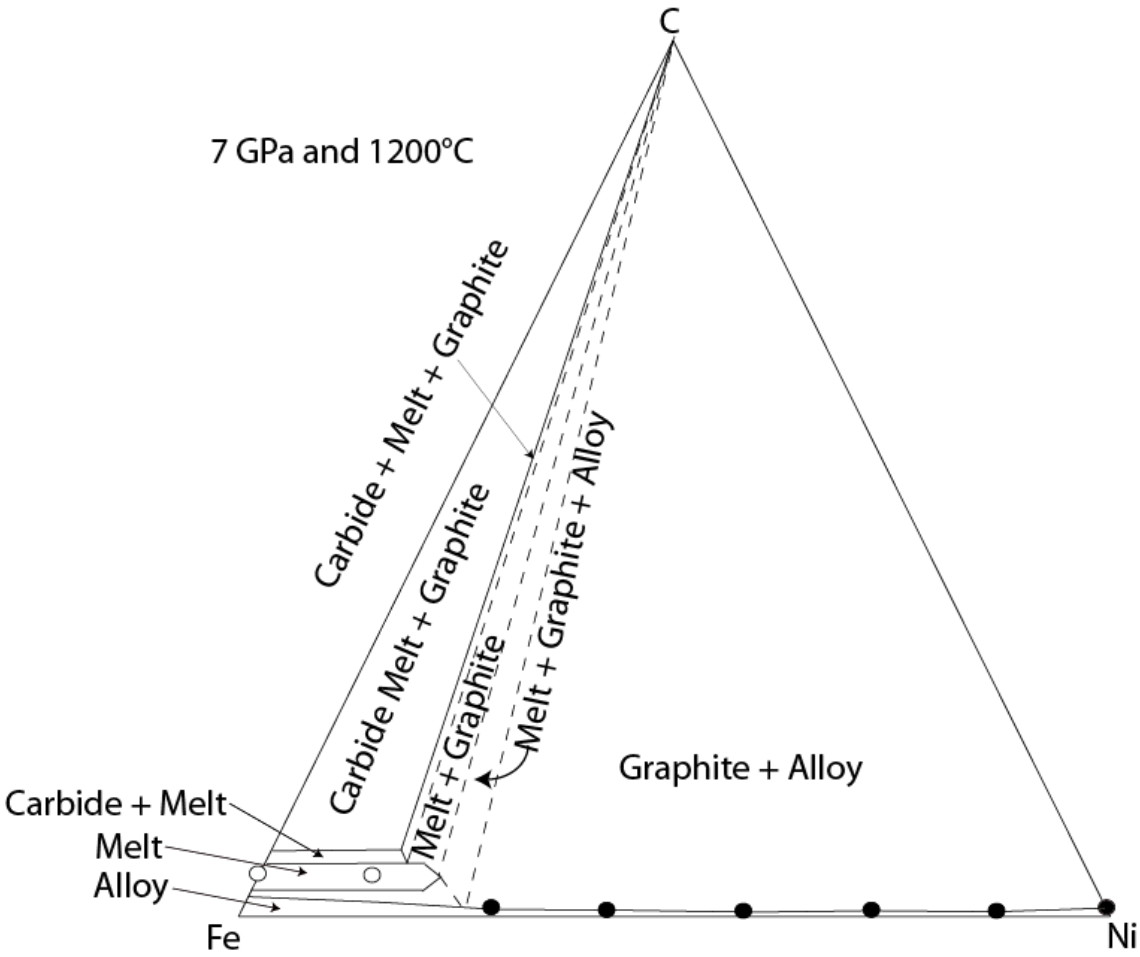

Figure 17. Fe-Ni-C phase diagram constructed from our experimental data for 7 GPa and 1200°C

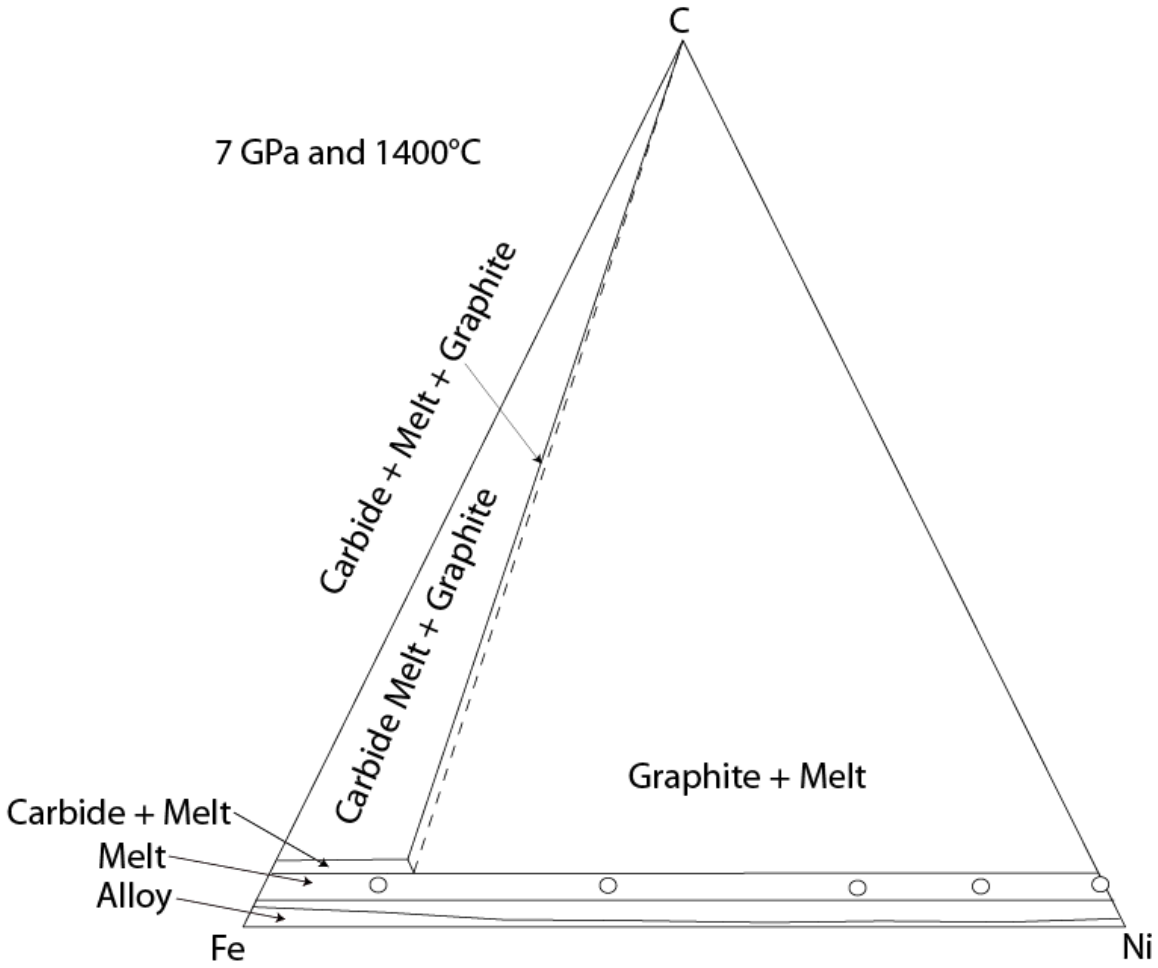

Figure 18. Fe-Ni-C phase diagram constructed from our experimental data for 7 GPa and 1400°C

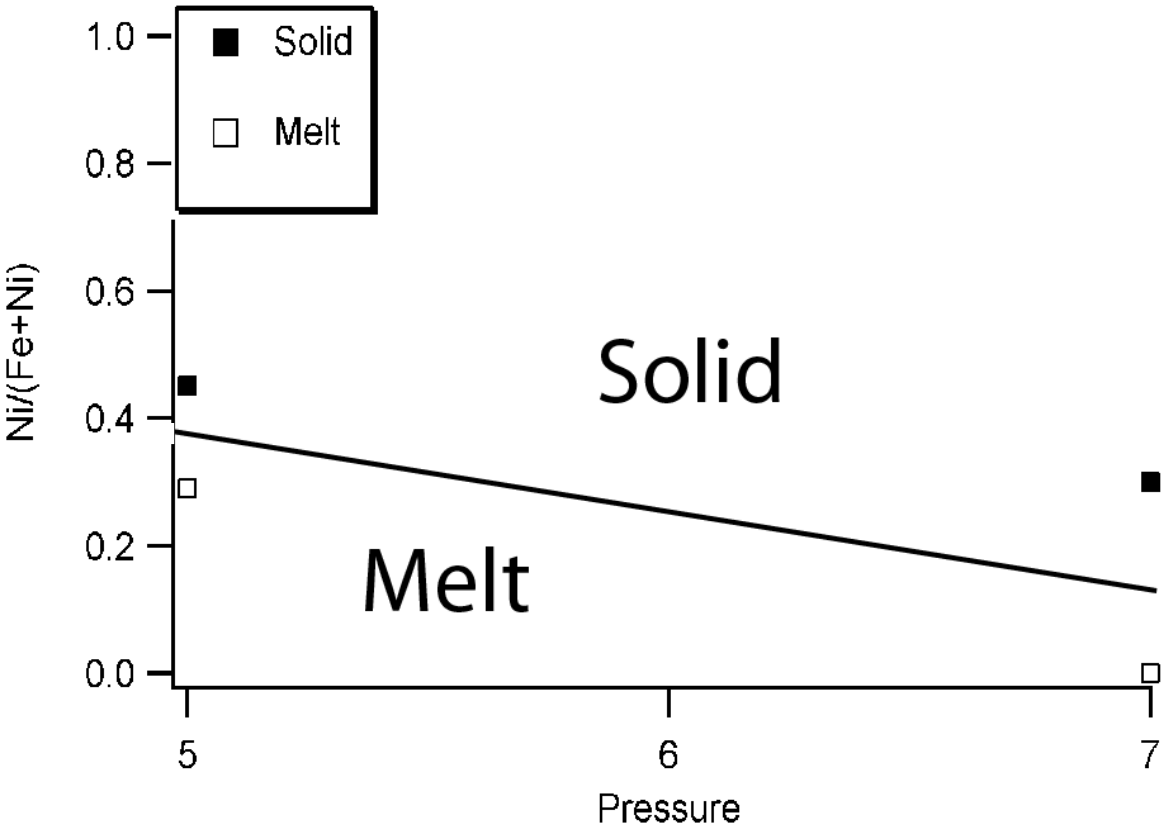

Figure 19. The melting point of changing alloy composition vs. pressure for 5 and 7 GPa 1200℃ experiments.

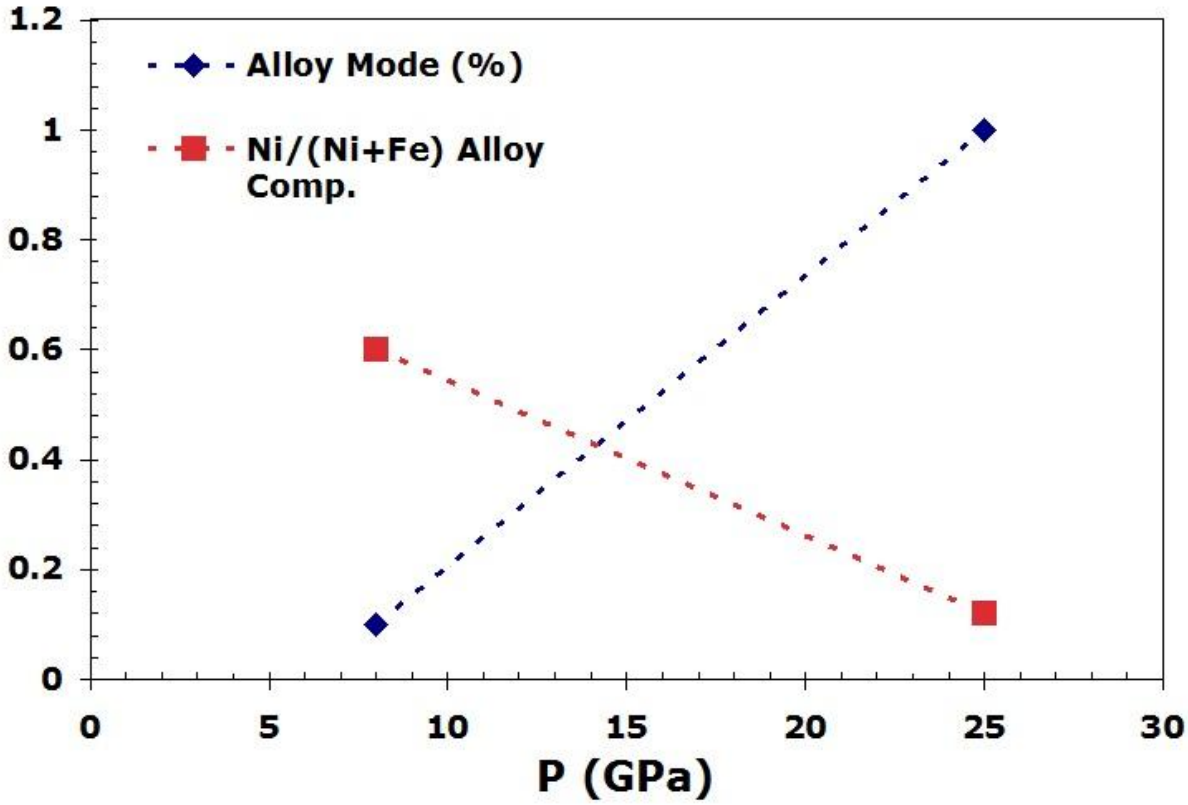

Figure 20. Changing alloy composition and modal abundance with depth. These are estimates of the first and last alloy to precipitate by Frost and McCammon. Graph drawn assuming changing alloy composition and modal abundance are linear.

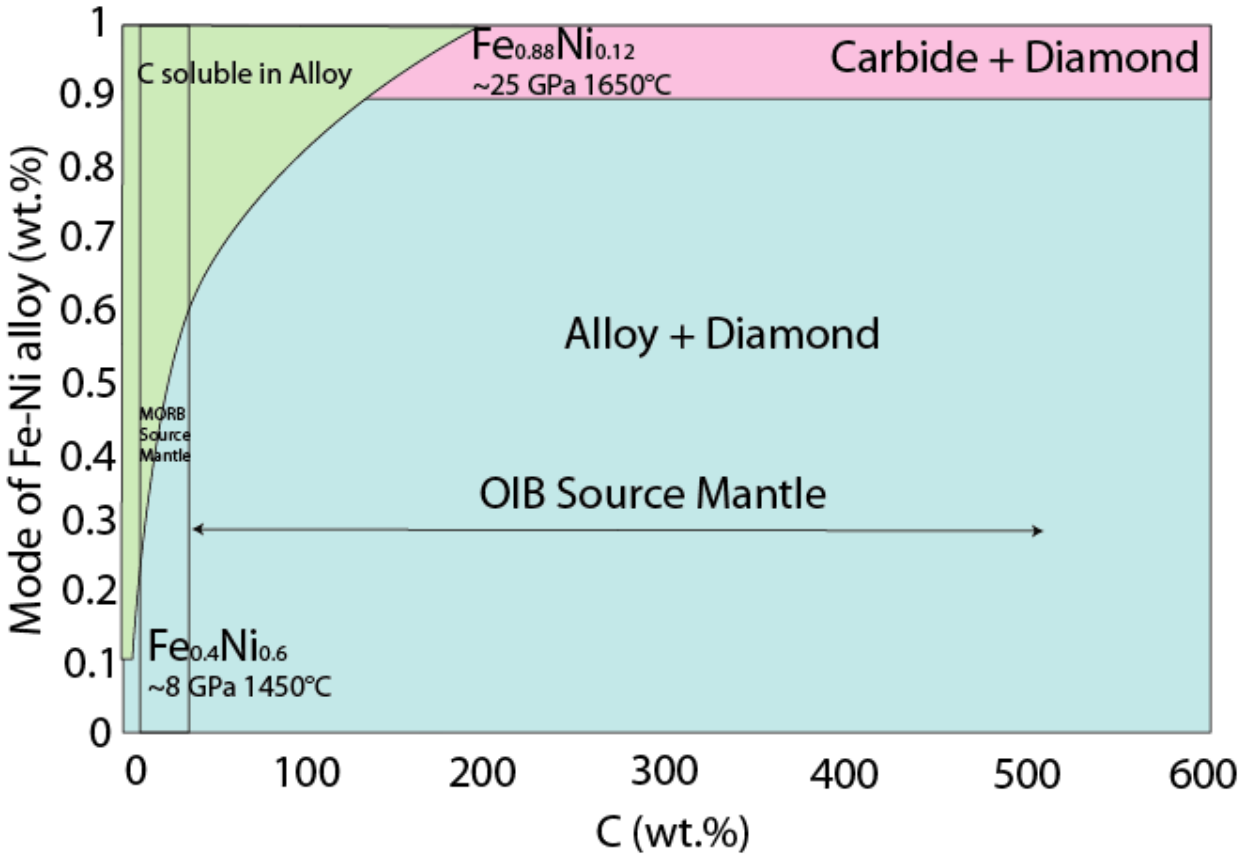

Figure 21. Graph of the maximum storage of C in Fe-Ni alloy from ~3 ppm in the upper mantle to ~200 ppm in the lower mantle. Boxed area shows the amount of carbon estimated in MORB source and the double ended arrow shows the amount of carbon estimated in an enriched mantle.

a.

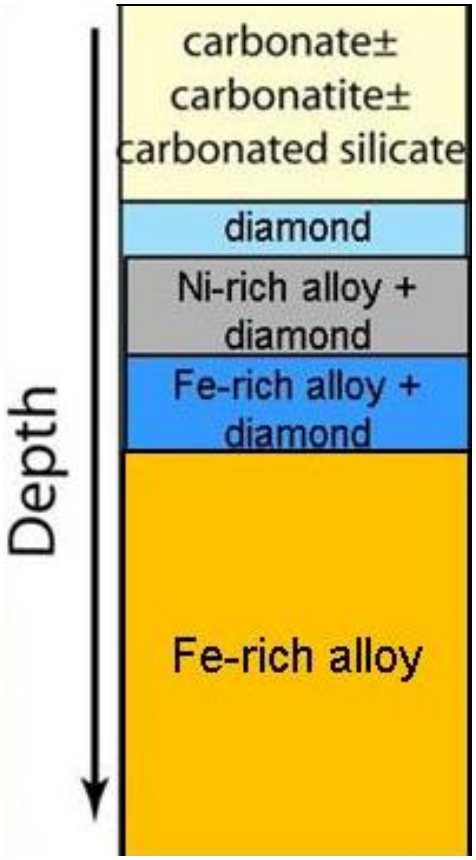

b.

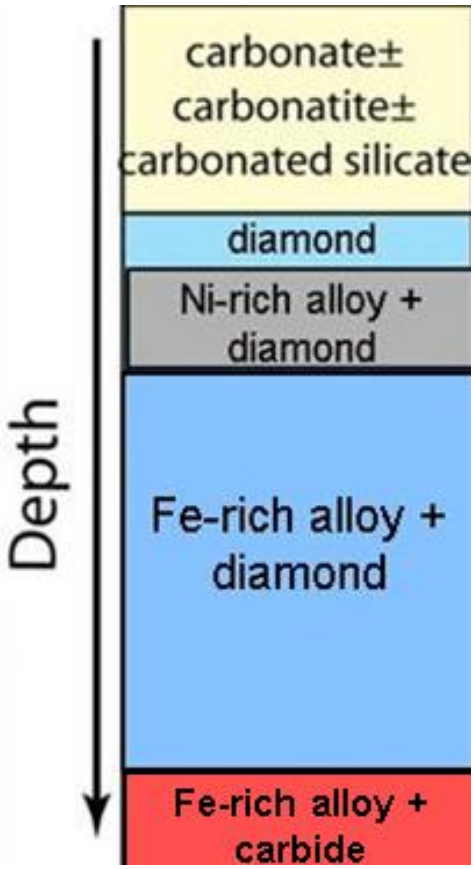

Figure 22. (a.) estimated scenario based on our solid alloy data of principal carbon phases in the mantle with depth for a MORB source mantle 10-30 ppm C. (b.) estimated scenario based on our solid alloy data of principal carbon phases in the mantle with depth for an enriched source mantle 30-500 ppm C.

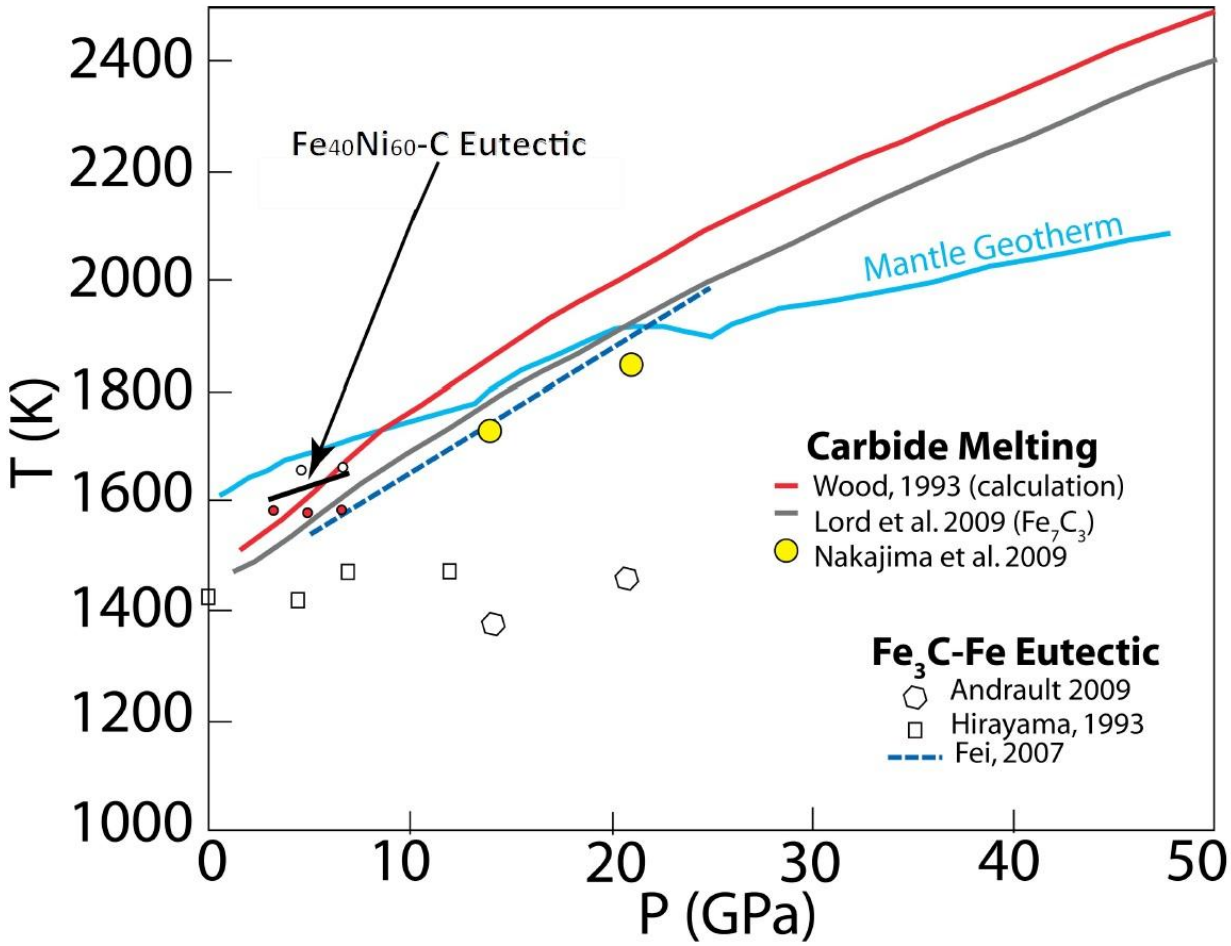

Figure 23. Our experimental eutectic temperature for $Fe_{0.4}Ni_{0.6}C$ drawn on a graph that shows the relationship between carbide melting and the mantle geotherm. All melting data are below the mantle geotherm up to more than 20 GPa. Mantle Geotherm redrawn after Stixrude and Lithgow-Bertelloni 2007.

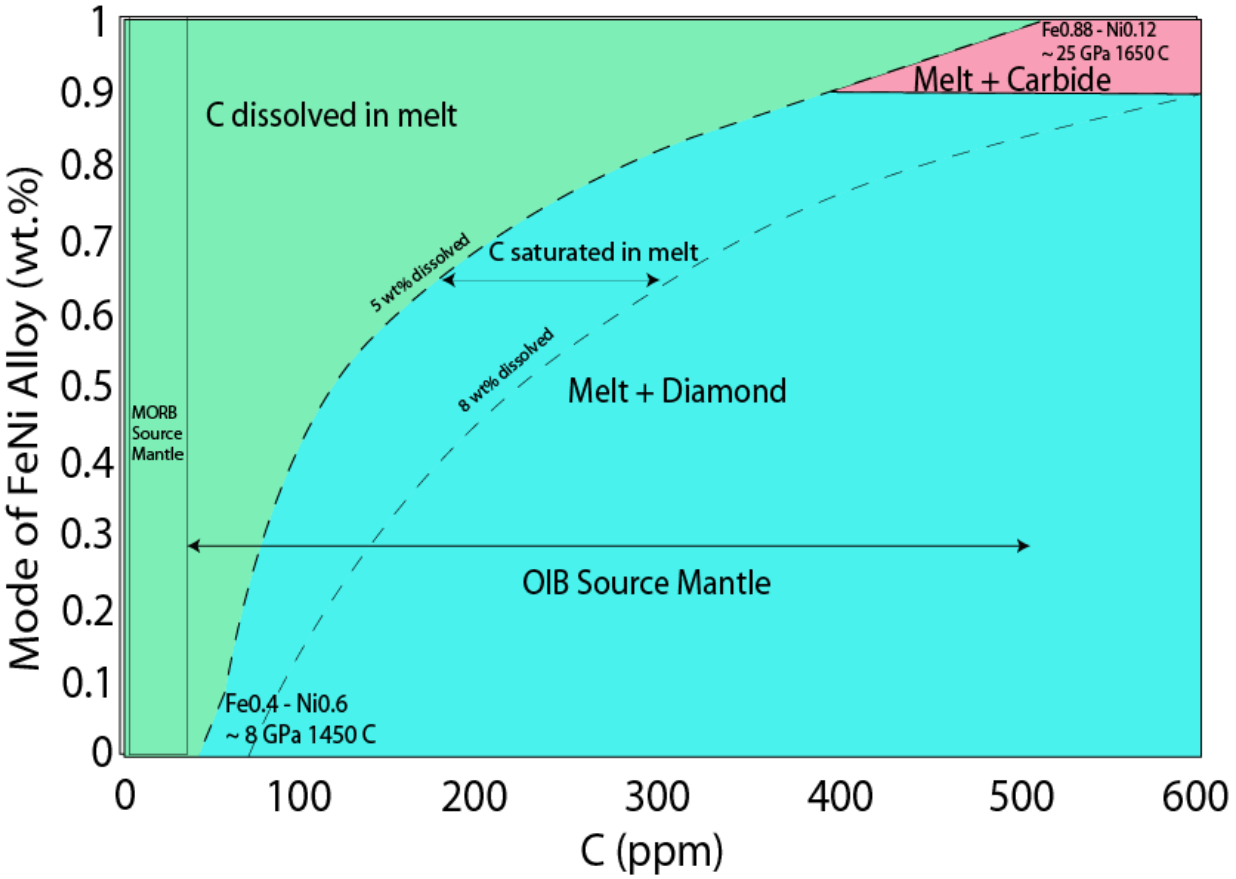

Figure 24. Graph of the amount of C dissolved in metal melts from 50 ppm in the upper mantle to 500 ppm in the lower mantle. Boxed area shows the amount of carbon estimated in MORB source and the double ended arrow shows the amount of carbon estimated in an enriched mantle. Other experimental results suggest that up to 6-8 wt.% C can be saturated in metal melts (Chabot et al. 2005; Dasgupta and Walker 2008) depending on the temperature.

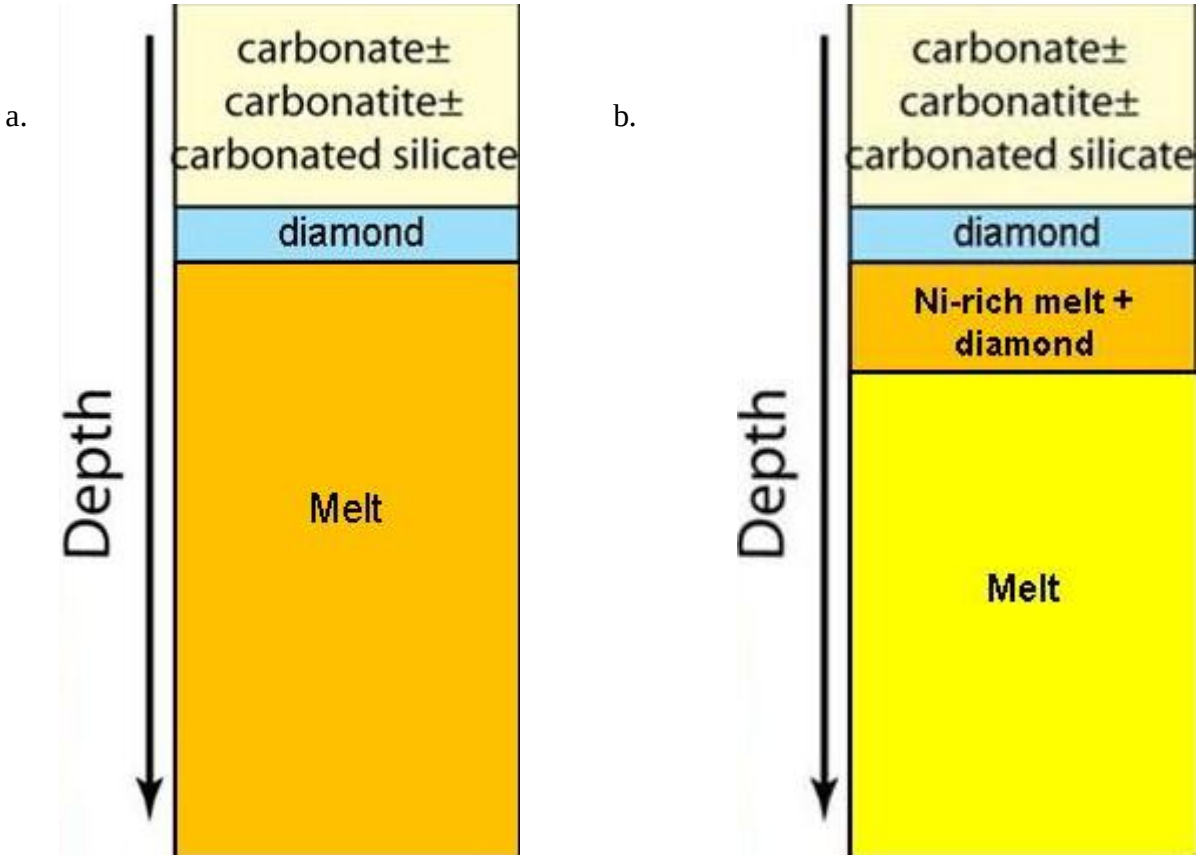

Figure 25. (a.) estimated scenario based on our melt data of principal carbon phases in the mantle with depth for a MORB source mantle 10-30 ppm C. (b.) estimated scenario based on our melt data of principal carbon phases in the mantle with depth for an enriched source mantle 30-500 ppm C.